

Dynamic polarization echoes in piezoelectric powders

K. Fossheim,* K. Kajimura,† T. G. Kazyaka, R. L. Melcher, and N. S. Shiren

IBM Thomas J. Watson Research Center, Yorktown Heights, New York 10598

(Received 9 September 1977)

The phenomenon of dynamic polarization echoes has been studied in powders of several piezoelectric materials at frequencies in the VHF band and in the *C*, *X*, and *Ku* microwave bands. The phenomenon is found to be a consequence of the anharmonicity associated with the mechanical oscillations of the individual particles of the powder. The phenomenon does not result from a parametric coupling of the applied rf fields to the mechanical-oscillator modes as might be expected by analogy to spin echoes and other types of polarization echoes. The anharmonic-oscillator model including damping has been developed in the small-signal limit for finite pulse widths. Although different sources of the anharmonicity cannot be distinguished in this limit, the experimental data unambiguously distinguish between the anharmonic-oscillator model and the parametric field-mode interaction. Under most experimental conditions the small-signal limit is not valid and the echo shapes, dependence on pulse amplitudes, and decay properties exhibit complex behavior. The quantitative understanding of this behavior awaits further detailed calculations. Multiple two-pulse echoes are detected at high rf powers. In the anharmonic-oscillator model multiple echoes arise naturally and the predicted decay behavior is in agreement with experiment. However the decay time is found to be strongly influenced by damage on the surface of the individual particles and by gases or liquids which surround the particles. Measurements of T_2^{-1} in a variety of gases with different acoustical impedances are in agreement with a simple calculation based upon the acoustical impedance mismatch between the solid and the gas. Measurements of T_2^{-1} versus frequency substantiate this model and indicate that the decay mechanism is internal to the particles when immersed in a high vacuum. Measurements in diluted samples demonstrate that interparticle interactions play no role in the echo formation process or in the observed echo behavior.

I. INTRODUCTION

Echo phenomena have been observed in a wide range of physical systems. In addition to the original work on nuclear¹ and electron^{2,3} spin echoes, several other diverse nonlinear systems have been shown to exhibit related phenomena. These include photon echoes from optical transitions in solids,⁴ magnetostatic echoes in yttrium iron garnet (YIG),⁵ cyclotron echoes in a plasma,⁶ echoes from molecular transitions in a gas,⁷ ultrasonic spin echoes,⁸ and phonon or polarization echoes of several types involving propagating elastic waves in piezoelectric crystals⁹⁻¹² and glasses.¹³

Observations of polarization echoes have also recently been made in powder samples consisting of a large number of small single-crystal particles of magnetoelastic,^{14,15} normal metallic,¹⁶⁻²⁰ superconducting,^{21,22,18} and piezoelectric²³⁻⁴⁶ materials. Powder echoes can be separated into two general types.^{43,46} "Static" or "memory" echoes are those for which the relaxation time T_1 , of the three-pulse stimulated echo exceeds the lifetime of any reasonable dynamic process. "Dynamic" echoes possess relaxation times which are related to some inherent dynamic behavior of the particles. This paper is concerned only with the dynamic echoes in powders.

Following a proposal by Gould⁴⁷ all echo phenomena can be separated into one of two classes ac-

ording to the type of nonlinear mechanism responsible for echoes. In "parametric field-mode" interaction systems the applied field of the second pulse interacts with the modes excited by the first pulse to cause phase reversal and echo formation. In "anharmonic-oscillator" systems the different oscillator modes are either nonlinearly coupled to one another, or, alternatively, there may be a single anharmonic mode of oscillation. Either of these nonlinearities can cause the subsequent echo formation.

The purpose of this paper is to present a rather detailed experimental study of the dynamic polarization echoes in powders of the piezoelectric materials SiO_2 , LiNbO_3 , GaAs , and ZnO . A preliminary report of our results has been published elsewhere.⁴⁶ We shall conclude on the basis of these experiments and the theoretical concepts discussed in Sec. II that these systems belong to the anharmonic-oscillator class of echo phenomena.

A. Echo sequence

The pulse sequence used in the present work is indicated in Fig. 1. Radio frequency (VHF, 20–300 MHz) or microwave frequency (*C*, *X*, and *Ku* bands) electric field pulses of peak amplitudes E_1 , E_2 , and E_3 and widths Δ_1 , Δ_2 , and Δ_3 and all with the carrier frequency ω_0 , are applied to the powder sample at times $t=0$, τ , and T , respectively.

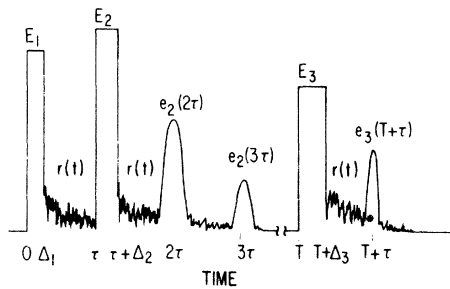


FIG. 1. Schematic of timing sequence for a typical three-pulse sequence showing occurrence of the ringing signal $r(t)$, and the echo signals $e_2(2\tau)$, $e_2(3\tau)$, and $e_3(T+\tau)$. The pulses and signals all have a common rf carrier frequency ω_0 . The signals and pulses have been demodulated as shown here.

After each pulse the sample is found to radiate an irregular quasicohherent ringing signal $r(t)$ which decays approximately exponentially. At the times $t = m\tau$, $m = 2, 3, 4, \dots$ the sample coherently radiates the two-pulse echoes $e_2(m\tau)$. At the times $t = nT + p\tau$, $n = 0, \pm 1, \pm 2, \dots$ and $p = 0, \pm 1, \pm 2, \dots$ (with the condition that $t > T$) the sample coherently radiates the three-pulse echoes $e_3(nT + p\tau)$. For large τ the two-pulse echo $e_2(2\tau)$ decays exponentially as $e_2(2\tau) \sim \exp(-2\tau/T_2)$, where T_2 is a phenomenological decay constant. Similarly, the three-pulse echo $e_3(T + \tau)$ decays as $\exp(-T/T_1)$, which can be used to define the decay constant T_1 .

In all cases considered here the constant T_2 is associated with the damping constant of mechanical oscillations of the individual powder particles. The relaxation time T_1 will be shown to have the same interpretation for dynamic echoes of the type considered here and is equal to $T_2/2$. For static or memory echoes in powders T_1 is determined by an entirely different mechanism although T_2 is again the mechanical damping constant.⁴³

B. Previous work on powder

The first observations of echoes in powders were in magnetoelastic ferrite powders.^{14,15} Although originally attributed to domain wall resonances,¹⁴ the echoes were later recognized to involve magnetoelastic modes of the individual particles of the powder.¹⁵ The nonlinear interaction responsible for echo formation was assumed to belong to the parametric field-mode class of mechanisms. Work on dynamic powder echoes in magnetoelastic materials has recently been extended to metallic ferromagnets²⁰ and to paramagnets.³³ Static powder echoes have also been observed in magnetoelastic powders.⁴³

Polarization echoes have also been studied in powders of both normal¹⁶⁻²⁰ and superconduct-

ing^{21,22,18} metals. Recent work in this area and reviews of the literature are included in Refs. 19 and 20. Conclusive evidence is not available to determine whether parametric field-mode or anharmonic-oscillator interactions dominate the echo-formation mechanisms in either magnetic or metallic powders.

Two groups in the Soviet Union were the first to report the observation of polarization echoes in piezoelectric materials.^{9,23} Popov and Krainik⁹ reported the detection of "anomalous" echoes in polycrystalline SbSI and Kessel' *et al.*²³ and reported the existence of similar echoes in ferroelectric powders. In a later publication²⁴ it was reported that some materials were capable of exhibiting echoes only when prepared in powder form. Thus the possibility arose that polarization echoes in powders are fundamentally different from those in single crystals. In Ref. 24 it was also shown that piezoelectricity rather than ferroelectricity^{9,23} is a necessary condition for the effect to occur in dielectrics. Other early work on powders included a study of the decay rate $\Gamma \equiv T_2^{-1}$ as a function of particle size in KH_2PO_4 (KDP).²⁵ However, because of the high rf frequency (1 GHz) and large particle size ($> 50\text{-}\mu\text{m}$ diam), the powder nature of the sample may have been immaterial to the echo-formation mechanism in these measurements.

During the past two years several short publications have reported on various properties of dynamic echoes in piezoelectric powders.²³⁻⁴⁶ These papers have conclusively demonstrated the important role played by the macroscopic mechanical modes of the individual particles in the echo-formation process. However, many of the other results appear to apply only to the specific experimental conditions used. These studies include the temperature,^{24,32,35,39,40} frequency,^{36,39,40} and particle size^{25,32} dependence of the decay constant T_2 , the temperature,^{30,32,33,35,39,40} frequency,²⁶ and particle size³⁷ dependence of the echo amplitude $e_2(2\tau)$, the rf power dependence,^{32,35} and others.

Simultaneous with this work on dynamic echoes came the discovery by several laboratories that the decay constant T_1 can under certain conditions exceed any reasonable dynamic relaxation time in a material.^{27,28,36,37,42-44} Although some confusion existed initially as to whether the static and dynamic echoes were different aspects of the same phenomenon, or distinct phenomena, it soon became clear that they did indeed arise through distinct physical processes. Two basic models for the long decay time T_1 of the static echoes have been proposed. One involves the formation of a static internal polarization or deformation of the individual particles as a consequence of the application

of a two-pulse sequence; T_1 is interpreted as the lifetime of the polarization.^{27,28,34,36} This process is quite similar to that responsible for holographic polarization echoes in single-crystal piezoelectric semiconductors.^{11,12} The second involves the physical rotation of individual particles due to the torque exerted by the second pulse on the oscillating dipole excited by the first pulse.^{37,43} In this mechanism the phase of the oscillation at the beginning of the second pulse is "stored" as the angle through which the particle rotates. This torque-rotation model appears to be gaining acceptance^{42,44,45} although the published experimental evidence is not conclusive.

The theoretical understanding of the dynamical echoes in powders was not much clearer until recently. Kessel *et al.*²³ proposed that the echoes could be explained by the existence of an electric dipole proportional to the third power of the deformation (i.e., strain). Although the physical origin of such a property was not elaborated upon, it would fall into the anharmonic-oscillator category. Some later papers implicitly assumed that parametric field-mode interactions similar to that proposed for single crystals⁴⁸ were dominant.^{31,34,35} Others made no suggestion as to the origin of echoes. In one paper an anharmonic-lattice potential was transformed into a parametric field-mode interaction during the second applied pulse.³⁰ This model requires that the frequency of the second pulse is twice the natural oscillation frequency of the particles. Smolenskii *et al.*³⁶ and Laikhtman⁴¹ have recently argued that anharmonic-oscillator mechanisms should be much more effective than the parametric field-mode interactions considered previously.^{31,34,35} However, they do not explicitly discuss the qualitatively different decay behavior expected of an anharmonic-oscillator echo system.

In a preliminary report of the present work we showed that only the anharmonic-oscillator mechanism is consistent with the experimental results in SiO_2 , LiNbO_3 , GaAs , and ZnO .⁴⁶ The conclusive evidence is the behavior of the echo amplitude as a function of pulse separation τ . In the anharmonic-oscillator case the echo builds up from zero for $\tau=0$ to a maximum before decaying exponentially for large τ . Echoes from a parametric field-mode interaction decay monotonically from a maximum for $\tau=0$ (with the exception of certain singular cases involving the interference of different echo modes⁴⁹).

C. Outline of remainder of this paper

The main emphasis of the present work will be the establishment of a more complete picture of the experimental facts concerning dynamic polar-

ization echoes in piezoelectric powders. In Sec. II we present a discussion of the relevant theoretical concepts including the distinction between anharmonic oscillators and parametric field-mode interactions. We also carry out calculations of a specific anharmonic-oscillator model using pulses of finite width valid only in the small-signal limit and using δ -function pulses in the large-signal limit. Section III is devoted to the details of the experimental methods used to acquire the data which are described in Secs. IV and V. A summary of the results and conclusions to be drawn from the work reported here is presented in Sec. VI.

II. THEORY

All echo phenomena are inherently nonlinear.⁵⁰⁻⁵³ In order to understand the formation of echoes by a particular system, it is necessary to have a model of the responsible nonlinear mechanism and to solve the relevant nonlinear equations. Because the linear response of the system can serve as a useful guide, we choose, in Sec. IIA below, to discuss in some detail the linear response to an applied electric field of a sample consisting of a large but finite number of piezoelectric particles. In Sec. IIB we present a general discussion of nonlinear mechanisms responsible for echo formation. In particular we distinguish between "parametric field-mode" type interactions and "anharmonic-oscillator" mechanisms. Echo phenomena resulting from fourth-order lattice anharmonicity of the particles are discussed in Sec. IIC. There we treat, firstly, the small-signal limit which takes into account the finite width of the applied pulses. Secondly, we treat the large signal limit using δ -function pulses.

A. Linear response

Although the linear response of a single piezoelectric particle is well understood^{54,55} for a limited number of simple geometries, we review it here in order to (i) develop notation and formalism for later use when we discuss the nonlinear response of such a particle, and (ii) to arrive at an explanation of the linear response of a sample consisting of a large number of such particles.

We approximate an irregularly shaped, randomly oriented piezoelectric particle with its complicated electromechanical mode structure by a thin platelet of thickness $2b$ and cross-sectional area A and we consider only thickness vibrations of the platelet. The orientation of the normal to the platelet relative to the applied field is given by the angle θ and it is assumed that the normal component of the applied field $E \cos\theta$ couples to the thickness vibrations of the platelet with the linear piezo-

electric constant e . We assume that the electrodes producing the applied field are at a sufficient distance from the particle that the field outside the particle is just $E = V/d$, where V is the voltage applied to the electrodes and d is the electrode spacing. Further, when calculating the response of a large number of particles in a single circuit, we shall treat each particle independently of the others, neglecting any particle-particle interactions.

The internal energy density of the platelet for this one-dimensional linear problem may be written

$$U_L = \frac{1}{2}c_2S^2 - eE_{1n}S - \frac{1}{2}\epsilon E_{1n}^2. \quad (1)$$

Here, c_2 , e , and ϵ are, respectively, the appropriate second-order elastic constant, the piezoelectric constant, and the dielectric constant of the material. The elastic strain of the thickness mode is S , and E_{1n} is the component of the internal field normal to the platelet surface. The piezoelectric equations of state take the form

$$T = \frac{\partial U_L}{\partial S} = c_2S - eE_{1n}, \quad (2a)$$

$$D = -\frac{\partial U_L}{\partial E_{1n}} = \epsilon E_{1n} + eS, \quad (2b)$$

where D is the electric displacement and T is the stress. The damped-wave equation for the elastic-displacement field $u(x, t)$, where $S = \partial u(x, t)/\partial x$, is given by

$$\ddot{u} + 2\Gamma\dot{u} = \frac{1}{\rho} \frac{\partial T}{\partial x} = \frac{c_2}{\rho} u_{xx} - \frac{1}{\rho} \frac{\partial}{\partial x} (eE_{1n}), \quad (3)$$

where $\Gamma \equiv T_2^{-1}$ is the damping constant $\dot{u} \equiv \partial u(x, t)/\partial t$, $\ddot{u} \equiv \partial^2 u(x, t)/\partial t^2$, and $u_{xx} \equiv \partial^2 u(x, t)/\partial x^2$.

We take the field E_{1n} to be oscillatory $\{-\exp[-i\omega_0(t-t_0)]\}$ with a slowly varying amplitude. The solution to Eq. (3) is taken to have the form

$$u(x, t) = a(t)m(x)e^{-i\omega_0(t-t_0)}, \quad (4a)$$

where $a(t)$ is a dimensionless slowly varying amplitude and $m(x)$ is a real, odd, normal-mode function normalized according to

$$V^{-1} \int m^2 dV = \frac{1}{2}b^2\delta, \quad (4b)$$

where the integral is over the volume V of the particle and δ is a normalization constant. The second term on the right-hand side of Eq. (3) can be evaluated by noting that $eE_{1n}(x, t)$ is discontinuous at the surface ($x = \pm b$) of the platelet

$$eE_{1n}(x, t) = eE_{1n}(x, t)[U(x+b) - U(x-b)] \quad (5a)$$

and its gradient is given by

$$\begin{aligned} \frac{\partial}{\partial x} [eE_{1n}(x, t)] &= e \frac{\partial E_{1n}(x, t)}{\partial x} [U(x+b) - U(x-b)] \\ &\quad + eE_{1n}(\pm b, t)[\delta(x+b) - \delta(x-b)]. \end{aligned} \quad (5b)$$

Here the unit step function $U(x) = 1$ if $x > 0$ and $U(x) = 0$ if $x < 0$, and $\delta(x)$ is the Dirac δ function.

Making use of Poisson's equation within the particle

$$\frac{\partial D}{\partial x} = 0 = \epsilon \frac{\partial E_{1n}}{\partial x} + e \frac{\partial S}{\partial x}, \quad (6)$$

the resulting equation for the amplitude $a(t)$ in the slowly varying envelope approximation is given by

$$\dot{a} + [\Gamma - i(\omega_0 - \Omega)]a = i\beta E_{1n}(\pm b, t)e^{i\omega_0(t-t_0)}, \quad (7a)$$

where the piezoelectrically stiffened normal-mode frequency is given by

$$\Omega^2 = -\frac{c_2(1+K^2)}{\rho} \frac{\int mm_{xx}dV}{\int m^2dV} = \frac{c_2(1+K^2)}{\rho} k^2. \quad (7b)$$

The second form of Eq. (7b) is obtained by taking $m(x)$ to be the simple, odd, periodic function

$$m(x) = b \sin kx. \quad (7c)$$

Here, k is the wave vector of the normal mode. The constant β in Eq. (7a) is given by

$$\beta = \frac{e}{2\rho\omega_0} \frac{m(b)}{b^2\delta}. \quad (7d)$$

From Eqs. (4b) and (7c) one finds

$$\delta = 1 - \sin 2kb / 2kb. \quad (7e)$$

The electromechanical coupling constant is given by

$$K^2 = e^2/\epsilon c_2. \quad (7f)$$

The boundary conditions at the surfaces of the platelet ($x = \pm b$) are: (i) the normal component of the electric displacement D is continuous; and (ii) the surface is stress free $T = 0$. Their application leads to $\delta \approx 1$ and to an expression for the normal component of the internal field at the surface $E_{1n}(\pm b, t)$, in terms of the normal component of the external applied field $E(t) \cos \theta$

$$E_{1n}(\pm b, t) = \frac{\epsilon_0/\epsilon}{1+K^2} \cos \theta E(t). \quad (8)$$

The solution to Eq. (7a) is

$$a(t) = \left(a(t_0) + i\beta \int_{t_0}^t E_{1n}(\pm b, T) \exp[\Gamma(T-t_0) + i\Omega(T-t_0)] dT \right) \exp\{-[\Gamma - i(\omega_0 - \Omega)](t-t_0)\}. \quad (9)$$

We take $E(t)$ to be the real part of a rectangular rf pulse of frequency ω_0 , amplitude E , and width Δ :

$$E(t) = iEe^{-i\omega_0(t-t_0)} [U(t-t_0) - U(t-t_0-\Delta)]. \quad (10)$$

Note that this specific form assumes a particular phase for $E(t)$. Although inconsequential for the present case of piezoelectric ringing, the precise choice of phase for the pulses does affect the phase of the echo as derived in Sec. II C below. The solution to Eq. (9) for $t > t_0 + \Delta$ can then be written

$$a(t, \omega, \theta) = [a(t_0, \omega, \theta) + a_\Delta(\omega, \theta, E, \Delta)] \times \exp\{-[\Gamma - i(\omega_0 - \Omega)](t - t_0)\}, \quad (11a)$$

where

$$a_\Delta(\omega, \theta, E, \Delta) = -\beta(\epsilon_0/[\epsilon_0/\epsilon/(1+K^2)]) \cos\theta E \Delta G(\xi), \quad (11b)$$

$$G(\xi) \equiv (\sin\xi/\xi)e^{-i\xi}, \quad (11c)$$

$$\xi \equiv (\omega + i\Gamma)\frac{1}{2}\Delta, \quad (11d)$$

and

$$\omega \equiv \omega_0 - \Omega. \quad (11e)$$

Here we have neglected sum frequency terms in $\omega_0 + \Omega$ corresponding to antiresonance.

The electric dipole $\vec{p}(t; \omega, \theta)$ associated with the oscillating platelet is given by

$$\begin{aligned} \vec{p}(t, \omega, \theta) &= \int \vec{P}(x, t, \omega, \theta) dV \\ &= \int e : S(x, t, \omega, \theta) dV, \end{aligned} \quad (12)$$

where $\vec{P}(x, \omega, \theta)$ is the piezoelectric polarization of the platelet. Using the difference frequency ω as a particle-mode label, the voltage response of a circuit containing a sample consisting of many particles is

$$V(t) = \sum_{\omega} v_{\omega} = \sum_{\omega} \vec{p}(t, \omega, \theta) \cdot \hat{e} G_R(\omega), \quad (13)$$

where \hat{e} is a unit vector in the direction of the electric field mode of the circuit and $G_R(\omega)$ represents the rf frequency response of the circuit and receiver. The sum \sum_{ω} is over all modes of all particles of the sample, the modes being labeled by the difference frequency ω .

On demodulation by video detection the receiver output is given by

$$V_{vid}(t) = \langle |\bar{V}(t)| \rangle, \quad (14)$$

where $\langle |\bar{V}| \rangle$ denotes the time average over the video bandwidth of the absolute value of the quantity enclosed.

It is useful to evaluate Eq. (14) for a large but finite number of particles. Taking the rf bandwidth to be infinite [$G_R = G_R(0)$] and the video band

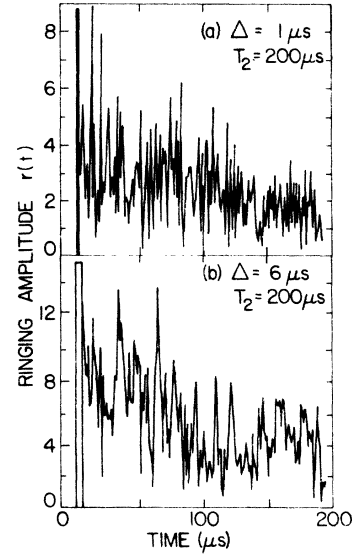


FIG. 2. Evaluation of the ringing signal, Eqs. (13) and (14), for 4000 particles whose natural frequencies are randomly chosen within $-5 \times 10^6 \leq \omega/2\pi \leq 5 \times 10^6$ Hz. Decay time $T_2 = 200 \mu s$ and pulse widths $\Delta = 1$ and $6 \mu s$.

width to be much less than ω_0 , and assuming for convenience that b and θ are the same for all particles, the video response for 4000 particles whose difference frequencies ω are randomly chosen within $-5 \times 10^6 \leq \omega/2\pi \leq 5 \times 10^6$ Hz has been evaluated and plotted in Fig. 2 for pulse widths $\Delta = 1 \times 10^{-6} \mu s$ and $\Delta = 6 \times 10^{-6} \mu s$. The essential features of these plots are: (i) the envelope of the irregular "ringing" signal decays as $\exp[-\Gamma(t - t_0)]$; (ii) the details of the signal are dependent upon the exact choice of the random values of ω ; and (iii) for wider pulse widths lower-frequency components appear in the signal [compare Fig. 2(b) with Fig. 2(a)].

The calculated signal amplitude is clearly proportional to the applied field strength, whereas its calculated dependence on the pulse width is more complicated as indicated in Eqs. (11). In Fig. 3 the calculated dependence of the signal amplitude on the pulse width is shown. The pulse-width dependence is determined by the explicit factor of Δ in Eq. (11a) as well as the Δ dependence of the effective Fourier spectrum of the pulse [Eq. (11c)]. As the pulse width increases the width of the pulse-frequency spectrum decreases thus affecting fewer particles, whereas those particles with $\omega \leq \Delta^{-1}$ are excited more strongly.

The dependence of the ringing signal on the drive frequency ω_0 can be easily deduced from Eqs. (11) and (13). When a reasonably well-defined particle size is used, the platelet width b can be factored out of the sum over ω . Further, assuming that the

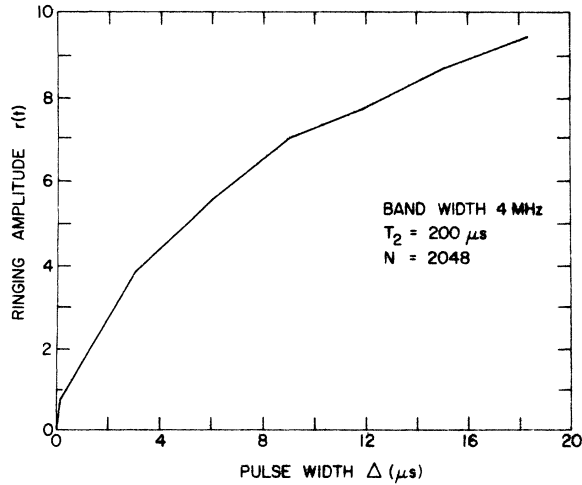


FIG. 3. Dependence of the ringing amplitude $r(t)$ on pulse width Δ for 2048 particles and a receiver bandwidth of 4 MHz. The natural frequencies of the particles were chosen as in Fig. 2.

density of particle modes is reasonably smooth over the width Δ^{-1} of the Fourier spectrum of the applied pulse [Eq. (11c)] the dependence of the ringing amplitude on ω_0 is given entirely by the density of modes $G_\omega(\omega)$; all other frequency factors cancel. The existence of an upper limit to the particle size results in a cutoff frequency $\Omega_c \approx \pi\nu/b$ below which $G_\omega(\omega) \rightarrow 0$ and the sample does not respond. In general there will exist no corresponding high-frequency cutoff in $G_\omega(\omega)$ be-

$$V(t) = -ie\omega_0 A G_\omega(0) m(b) \int_0^{\pi} \sin\theta \cos\theta d\theta \int_{-\infty}^{\infty} a(t, \omega, \theta) \exp[-i\omega_0(t-t_0)] G_R(\omega) d\omega. \quad (16)$$

With

$$G_R(\omega) = G_R(0) / [1 + (\omega/\omega_B)^2], \quad (17)$$

and using the linear solution given by Eq. (11a) with $a(t_0, \omega, \theta) = 0$ we obtain

$$V(t) = -\frac{\pi}{3} \left(\frac{K^2}{1+K^2} \right) \epsilon_0 v^2 \frac{Am^2(b)}{b^3} E \Delta G_\omega(0) G_R(0) G(\xi_B) \times \exp[-i\omega_0(t-t_0) - (\Gamma + \omega_B)(t-t_0)], \quad (18)$$

where $\xi_B = \xi(\omega = i\omega_B) = \frac{1}{2}i(\omega_B + \Gamma)\Delta$. In the experimentally interesting case of $\omega_B \gg \Gamma$ we have that $V(t)$ is just the ringing of the electrical circuit at the drive frequency ω_0 damped by the circuit band width ω_B . In the limit $\omega_B \rightarrow \infty$ we have $V(t) \rightarrow 0$. Thus, as expected in the limit of a very large number of piezoactive vibrational modes, complete phase cancellation of the particle oscillations occurs and no signal is detected.

In our discussion of the coherent nonlinear re-

cause of the excitation of higher harmonics.

Contrary to existing statements,³⁴ the ringing signal considered here is not an analog of the free-induction decay of a spin system. The ringing is a linear and essentially incoherent signal which vanishes in the limit of an infinite number of particles because of phase cancellation of the signals from the individual oscillators. The free-induction decay of a spin system is coherent and consequently does not vanish as the number of spins increases.

In Sec. IV A we shall compare the above calculations for the ringing signal to experiment and conclude that good agreement is obtained.

The irregular ringing signal described here is the remnant of the incomplete phase cancellation of the oscillating dipoles associated with the modes of each particle. In the limit of an infinite number of modes the sum in Eq. (13) can be replaced by a double integral over the mode distribution $G_\omega(\omega)$, and the solid angle $\sin\theta d\varphi d\theta$, where φ is the azimuthal angle in the plane normal to the field. Taking the distribution of particle orientations to be uniform [$G_{\theta\varphi}(\theta, \varphi) \equiv 1/(4\pi)$] we find

$$\sum_{\omega} v_{\omega} = \frac{1}{4\pi} \int_0^{2\pi} d\varphi \int_0^{\pi} \sin\theta d\theta \int_{-\infty}^{\infty} G_\omega(\omega) v_{\omega} d\omega. \quad (15)$$

Taking $G_\omega(\omega)$ to be slowly varying with respect to Δ^{-1} and to G_R we find from Eqs. (11)–(13) and (15)

sponse of the powder sample we shall make use of Eq. (16) with $a(t, \omega, \theta)$ representing the solution to the appropriate nonlinear wave equation.

B. Classification of nonlinearities

Gould⁴⁷ has distinguished between two general types of nonlinear mechanisms which can give rise to echo phenomena in classical oscillator systems: (i) "Field-mode" interactions are those in which the applied field couples parametrically to the previously excited modes of the system causing phase reversal and subsequent echo formation. (ii) "Anharmonic-oscillator" interactions exist even in oscillator systems which interact linearly with the applied field. However, either the different free-oscillation modes are coupled anharmonically (e.g., in harmonic generation) or the free oscillations exhibit nonlinear amplitude-dependent dispersion and/or damping. In the fol-

lowing paragraphs we discuss these two classes of interactions and give examples of each. One of the conclusions of this paper is that the nonlinear mechanism(s) responsible for dynamic polarization echoes in piezoelectric powders belong to the anharmonic-oscillator class.

1. Field-mode interactions

In many physical systems there exists a parametric coupling between an applied electromagnetic field and previously excited normal modes of the system. The first pulse (at $t=0$) of a two-pulse echo sequence in such a system excites normal modes. The second pulse (at $t=\tau$) interacts parametrically with these modes so as to reverse their phases. Thus the dephasing occurring during the interval $0 < t < \tau$ is recovered during the interval $\tau < t < 2\tau$. Consequently, the modes coherently radiate an echo at $t=2\tau$. Since the phase reversal occurs only during the second pulse at $t=\tau$, the echo amplitude (neglecting damping) is independent of the pulse separation τ . On taking damping into account, the echo amplitude decreases from a finite value monotonically with increasing τ from its maximum value at $\tau=0$.

Spin echoes represent the most familiar example of echoes resulting from a parametric field-mode interaction. The interaction of a spin S with the applied field H is described by the Bloch equations, which are parametric in H_{rf} . Similar considerations hold for photon echoes and phonon echoes in paramagnets and glasses.⁵⁶

Parametric backward wave interactions giving rise to polarization echoes in crystals represent another form of parametric field-mode interaction. In one class of such processes the interaction arises from nonlinear piezoelectricity of the form $U = \frac{1}{2}\gamma_5 ES^2$, where γ_5 is a fifth-rank tensor.¹⁰ The resulting stress is $T = \gamma_5 ES$. A forward propagating strain wave $S \sim e^{-i(\omega t - kx)}$, and an applied field $E \sim e^{2i\omega t}$, at twice the frequency, lead to a backward propagating stress wave $T \sim e^{i(\omega t + kx)}$, which is detected as the echo. When the frequency of the field E and that of the strain wave S are equal, a nonlinear electrostrictive interaction has been proposed of the form $U = \frac{1}{2}\gamma_6 E^2 S^2$, where γ_6 is a sixth-rank tensor.⁴⁸ The magnitude of γ_6 is unknown and therefore it is difficult to assess the importance of this mechanism. This mechanism is considered in detail in the Appendix explicitly for powders. We note here only that it does not by itself give rise to multiple two-pulse echoes at $t = m\tau$, $m > 2$, nor does it give rise to a stimulated three-pulse echo.

A different parametric mechanism has been shown to be responsible for polarization echoes in

high-resistivity piezoelectric semiconductors when the field and the strain wave are at the same frequency.^{11,12} The field at frequency ω_0 causes ionization of charges trapped at shallow defect states to give a component to the conduction electron number density n which oscillates at $2\omega_0$. This number density then interacts with the longitudinal electric field $E_p \sim e^{-i(\omega t - kx)}$, of the forward propagating piezoactive strain wave via the drift current $J = q\mu E_p$, where q is the electronic charge and μ the mobility. Consequently, a backward current wave $J \sim e^{i(\omega t + kx)}$, and concomitantly a backward strain wave and echo are generated. A related mechanism is responsible for holographic echoes with long time storage capability in such materials.^{10,11}

Polarization echoes with very long time storage in piezoelectric powders constitute yet another echo phenomenon arising from a parametric field-mode interaction. The nonlinear mechanism has been proposed to be simply the torque exerted on an oscillating electric dipole by an applied rf electric field.^{37,42-45} The resulting mechanical reorientation of the individual particles effectively stores the phase of the individual particles at the instant ($t = \tau$) of application of the second pulse. The dependence of the excitation of a particle by a third pulse on the orientation of the particle causes the coherent radiation of the stimulated echo. A two-pulse echo is radiated in a similar manner. The present paper is concerned only with dynamic echoes in powders, processes which do not involve particle reorientation. By methods discussed in Sec. III the long-time storage effects have been suppressed in all experiments described in this paper.

2. Anharmonic-oscillator interactions

A system of oscillators which interact only linearly with applied fields can nonetheless exhibit echo phenomena if the oscillators are themselves anharmonic.⁴⁷ In a two-pulse echo sequence the first pulse serves simply to excite the oscillators and the second pulse does precisely the same. However, between the two pulses and, in particular, after the second pulse the oscillators behave anharmonically. In effect the anharmonic coupling between the oscillations excited by the first pulse and those excited by the second causes a cumulative phase reversal to occur after the second pulse, thus undoing the dephasing which occurred between the two pulses. At $t = 2\tau$ this reversal is complete and a coherent echo signal is radiated. Since the time interval $\tau < t < 2\tau$ is that during which the anharmonic interaction occurs, reducing τ to zero causes the integrated interaction to vanish and the echo amplitude must also go to zero.

Consequently the echo amplitude increases with increasing pulse separation τ in contrast to the behavior exhibited by echoes derived from parametric field-mode interactions. In practice, mode damping dominates the behavior for large τ . This causes the echo to initially increase with τ , reach a maximum, and finally decrease for large τ .

The three known examples of echoes from anharmonic oscillators are cyclotron echoes in plasmas,^{47,50,57} magnetostatic echoes in YIG⁵⁸⁻⁶⁰ and dynamic polarization echoes in powders.⁴⁶ The simplest consequences of anharmonicity are amplitude-dependent dispersion and damping. Additional effects such as harmonic generation cannot always be ruled out. The physical origin of the anharmonicity can be inherent to the system or be induced by defects of various types.

In Sec. II C we describe a model based upon pure lattice anharmonicity.

C. Anharmonic oscillator

Consider the nonlinear behavior resulting from lattice anharmonicity. The internal energy density U of a particle takes the form

$$U = U_L + U_{NL}, \quad (19)$$

where the linear term U_L is given by Eq. (1) and the nonlinear term U_{NL} can be written

$$U_{NL} = (1/3!)c_3 S^3 + (1/4!)c_4 S^4 + \dots \quad (20)$$

Here c_3 and c_4 are, respectively, the effective third- and fourth-order elastic constants. The nonlinear wave equation

$$\ddot{u} + 2\Gamma\dot{u} - \frac{c_2}{\rho}u_{xx} - \frac{c_3}{\rho}u_x u_{xx} - \frac{c_4}{2\rho}u_x^2 u_{xx} - \dots = -\frac{1}{\rho} \frac{\partial(eE_{1n})}{\partial x}. \quad (21)$$

The linear piezoelectric driving force on the right-hand side excites only those modes in the neighborhood of the applied rf frequency ω_0 . We refer to these directly excited modes as the "fundamental modes" and assume that for a given particle and frequency ω_0 only one such mode is excited. The nonlinear terms on the left-hand side of Eq. (21) cause amplitude-dependent phase shifts and damping of the fundamental modes as well as harmonic generation.

Rather than attempt to find a general solution of Eq. (21) we make the somewhat arbitrary simplification of retaining only the fourth-order anharmonicity. The higher-order terms can be dropped on the basis that they are small. The role of the third-order term in causing harmonic generation and echo formation has also been considered. We note here only that in the small-signal limit the results are similar to those obtained here from the

fourth-order term.

The lowest order the fourth-order anharmonicity causes nonlinear dispersion (phase shift) of the fundamental modes. Therefore, although odd harmonics are allowed by the boundary conditions of a thin platelet, we neglect all harmonic generation. Assuming a solution of the form given by Eq. (4a) we can derive in the slowly varying envelope approximation [see Eq. (7a)] the equation

$$\dot{a} + [\Gamma - i(\omega_0 - \Omega)]a - i\gamma|a|^2 a = i\beta E_{1n}(\pm b, t)e^{i\omega_0(t-t_0)}, \quad (22a)$$

where Ω and β are given, respectively, by Eqs. (7b) and (7d), and γ is defined by

$$\gamma = \frac{3}{4} \frac{c_4}{\rho\omega_0} \frac{\int mm_x^2 m_{xx} dV}{\int m^2 dV} = -\frac{3}{16} \frac{c_4}{\rho\omega_0} k^4 b^2, \quad (22b)$$

where the second form of Eq. (22b) arises specifically for the platelet geometry [see Eq. (7c)]. Equation (22a) explicitly ignores harmonic generation.

In the limit of $\gamma=0$ [see Eq. (9)] or in the limit of $E_{1n}(\pm b, t)=0$, Eq. (22a) can be solved exactly. In the discussion below we describe the echo formation process resulting from Eq. (22a) in (i) the small-signal limit for finite pulse widths, and in (ii) the large-signal limit for δ -function pulses.

1. Small-signal limit—Finite pulse widths

We restrict the analysis here to: (i) the small-signal limit correct only to first order in the nonlinear constant γ ; and to (ii) pulse widths Δ small compared to the damping time $T_2 = \Gamma^{-1}$, $\Gamma\Delta \ll 1$. In this case the nonlinearity can be neglected ($\gamma=0$) during the applied pulses. The solution [Eqs. (11a)–(11e)] of the linear driven equation [either Eq. (7a) or Eq. (22a) with $\gamma=0$] at the end of each applied pulse is then used as the initial condition for the solution of the freely oscillating [$E_{1n}(\pm b, t)=0$] nonlinear equation of motion described by Eq. (22a).

The exact solution of Eq. (22a) with the right-hand side set equal to zero is

$$a(t) = a(t_0) \exp\{-[\Gamma - i(\omega_0 - \Omega)](t - t_0) - \gamma/(\gamma - \gamma^*)\} \\ \times \ln[1 - i(\gamma - \gamma^*)/2\Gamma |a(t_0)|^2] \\ \times (1 - e^{-2\Gamma(t-t_0)}). \quad (23a)$$

Here we have specifically allowed γ to be complex and therefore are including possible nonlinear damping effects as well as the nonlinear dispersion arising from the real γ of Eq. (22b). To first order in both the real and imaginary parts of γ we have

$$a(t) = a(t_0) \exp\{-[\Gamma - i(\omega_0 - \Omega)](t - t_0)\} \\ \times \left[1 + i \frac{\gamma}{2\Gamma} |a(t_0)|^2 (1 - e^{-2\Gamma(t-t_0)}) \right]. \quad (23b)$$

To first order in γ , only the nonlinear behavior occurring after the second pulse of a two-pulse sequence is of importance. Applying Eqs. (11a)–(11e) for the excitation caused by both the first and the second pulses, the initial condition $a(t_0)$

$$V(t) = \frac{3}{160} G_R(0) c_4 \frac{K^4}{(1+K^2)^3} \left(\frac{1}{2}\omega_0 T_2\right) \frac{\epsilon_0}{\epsilon} \frac{\epsilon_0^2}{\rho^2} \frac{m^4(b)}{b^7} A G_\omega(0) \Delta_1 \Delta_2^2 E_1 E_2^2 \exp[-i\omega_0(t - 2\tau) - \Gamma(t + 2\Delta_2)] \\ \times (1 - e^{-2\Gamma(t-\tau-\Delta_2)}) \int_{-\infty}^{\infty} G_1^*(\xi_1) G_2^2(\xi_2) e^{i\omega(t-2\tau)} d\omega. \quad (25)$$

Here we have set $G_\omega(\omega) \simeq G_\omega(0)$ and $G_R(\omega) = G_R(0)$ and taken them out of the integral, and ξ_1 and ξ_2 correspond to ξ of Eq. (11d) for the first and second pulses, respectively.

Several significant conclusions can be drawn from the small-signal limit represented by Eq. (25). (i) The signal amplitude is proportional to the anharmonic coefficient c_4 , the square of the electromechanical coupling constant K^2 (when $K^2 \ll 1$), and the mechanical Q of the particles ($Q \simeq \omega_0 T_2/2$). (ii) The signal amplitude increases with the applied field amplitudes E_1 and E_2 as $E_1 E_2^2$. (iii) The dependence on the pulse separation τ is given by the exponential factors preceding the integral; for $\Gamma \Delta_2 \ll 1$ and $t = 2\tau$ it is given by $e^{-2\Gamma\tau}(1 - e^{-2\Gamma\tau})$. Thus for $\tau \rightarrow 0$, $V(t) \sim \tau$ and for $\tau \rightarrow \infty$, $V(t) \simeq e^{-2\Gamma\tau}$. (iv) The integral over ω in Eq. (25) is nonzero only for $t \simeq 2\tau$. To first order in c_4 , this 2τ echo is the only coherent signal radiated. (v) The echo shape is given by the evaluation of the integral over ω . Several representative echo shapes are given in Fig. 4. (vi) Allowing c_4 to be complex has no effect other than to shift the rf phase of the echo. Consequently, in the small-signal limit nonlinear absorption and dispersion of these general types are indistinguishable. The properties (ii), (iii), and (iv) can be used to compare this class of small-signal anharmonic-oscillator theories to experiment. We make this comparison in Sec. IV.

The validity of the small-signal solution can be seen from Eq. (23) to require that

$$L(E, \Delta, \omega, \theta, t) \equiv \left| \frac{i\gamma}{2\Gamma} |a(t_0)|^2 (1 - e^{-2\Gamma(t-t_0)}) \right| \ll 1. \quad (26)$$

Not only does L depend upon the applied pulse amplitude E and width Δ , but also on the relative

at $t_0 = \tau + \Delta_2$ for Eq. (23b) is found to be

$$a(t_0 = \tau + \Delta_2) = (a_{\Delta 1} e^{-(\Gamma+i\Omega)\tau} + a_{\Delta 2}) e^{-(\Gamma+i\Omega)\Delta_2}, \quad (24)$$

where $a_{\Delta 1}$ and $a_{\Delta 2}$ are the excitation amplitudes imparted by the first and second pulses, respectively, and are given by Eq. (11b).

On substituting Eqs. (23b) and (24) into Eq. (16) the following expression is obtained for the coherent voltage generated in the circuit after a two-pulse sequence

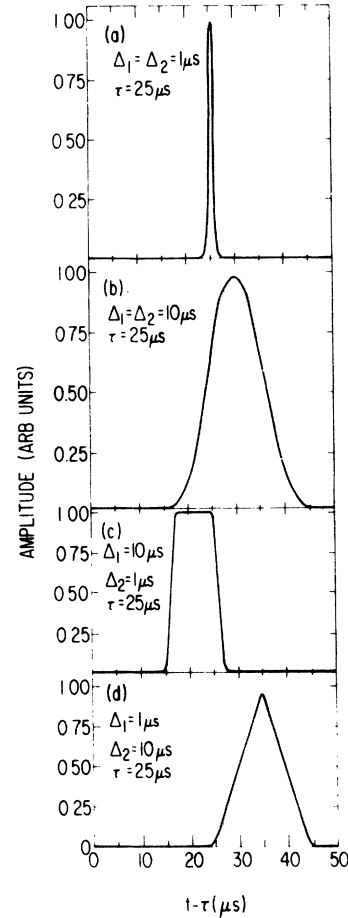


FIG. 4. Two-pulse echo shapes and positions computed from Eq. (25) valid for the anharmonic oscillator model in the small signal limit. Amplitude plotted vs $t - \tau$ with $\tau = 25 \mu s$, $T_2 = 1000 \mu s$, and (a) $\Delta_1 = \Delta_2 = 1 \mu s$, (b) $\Delta_1 = \Delta_2 = 10 \mu s$, (c) $\Delta_1 = 10 \mu s$ and $\Delta_2 = 1 \mu s$, and (d) $\Delta_1 = 1 \mu s$ and $\Delta_2 = 10 \mu s$.

mode frequency ω , the particle orientation θ , and the time t . Thus for a given applied pulse, some particles in a single sample may exhibit large-signal behavior while others satisfy the small-signal limit.

If, as a fairly realistic example, we choose $\theta = 0$, $\omega = 0$, $t \rightarrow \infty$, $Q = \frac{1}{2}\omega_0 T_2 = 10^5$, $E = 10^6$ V/m, $\Delta_1 = 10^{-6}$ s, $2\Gamma\Delta_1 \ll 1$, $K^2 = 0.25$, $\rho = 3 \times 10^3$ kg/m³, $b = 50 \times 10^{-6}$ m, $\epsilon_0/\epsilon = 1$, then we find that the small signal limit breaks down for $c_4 \geq 10^4 c_2$.

In order to extend the small signal result to arbitrarily large signals (i.e., higher applied fields), one should solve the full nonlinear inhomogeneous equation, Eq. (22a).

2. Large-signal limit— δ -function pulses

In the limit of δ -function applied pulses, the problem, as formulated by Eq. (22a), can be

$$a(t > \tau) = \{a_{\Delta 1} \exp[-(\Gamma + i\Omega)\tau + i(\gamma/2\Gamma)|a_{\Delta 1}|^2(1 - e^{-2\Gamma\tau})] + a_{\Delta 2}\} \exp\{-[\Gamma - i(\omega_0 - \Omega)](t - \tau)\} \\ \times \exp\{i(\gamma/2\Gamma)|a_{\Delta 1} \exp[-(\Gamma + i\Omega)\tau + i(\gamma/2\Gamma)|a_{\Delta 1}|^2(1 - e^{-2\Gamma\tau})] + a_{\Delta 2}\}^2(1 - e^{-2\Gamma(t-\tau)})\}. \quad (29)$$

Setting

$$\eta \equiv (\gamma/2\Gamma)2a_{\Delta 1}a_{\Delta 2}e^{-\Gamma\tau}(1 - e^{-2\Gamma(t-\tau)}), \quad (30a)$$

$$\Phi \equiv \Omega\tau - (\gamma/2\Gamma)|a_{\Delta 1}|^2(1 - e^{-2\Gamma\tau}), \quad (30b)$$

$$\delta_m = (\gamma/2\Gamma)\{a_{\Delta 2}^2(1 - e^{-2\Gamma(t-\tau)}) - a_{\Delta 1}^2[(m-1)(1 - e^{-2\Gamma\tau}) - e^{-2\Gamma\tau}(1 - e^{-2\Gamma(t-\tau)})]\}, \quad (30c)$$

$$V_{m\tau} = i^m \frac{1}{2} \left(\frac{K^2}{1+K^2} \right) \epsilon_0 \frac{c_2}{\rho} \frac{Am^2(b)}{b^3} \exp[-\Gamma(t-\tau) - i\omega_0(t-m\tau)]$$

$$\times \int_{-\pi}^{\pi} G_{\omega}(\omega) G_R(\omega) e^{i\omega(t-m\tau)} d\omega \int_0^{\pi} \sin\theta \cos^2\theta e^{i\delta_m(\theta)} [iA_1 J_m(\eta) e^{-\Gamma\tau} + A_2 J_{m-1}(\eta)] d\theta. \quad (31)$$

This result is similar to that obtained by others⁵² except that here we have included damping and have not neglected the phase factor $\delta_m(\theta)$ because of its dependence on the particle orientation θ . For large amplitudes $\delta_m(\theta)$ can exceed 2π and phase cancellation of the radiation of particles with different θ can occur. In addition, η is dependent upon θ . Thus the integral over θ in Eq. (31) has a significant effect on the echo behavior in the large-signal limit. As in Eq. (15) the solution given by Eq. (31) has assumed a uniform distribution of particle orientations. If only a single orientation were present in the sample, one would insert into the θ integral a δ function $\delta(\theta - \theta_0)$. In the small-signal limit [$\delta_m(\theta) \ll 2\pi$, $\eta(\theta) \ll 1$] there is no qualitative difference between these two ex-

solved exactly. Because of the infinitesimal pulse width the pulses only provide the initial condition for the solution to Eq. (22a) with $E_{in} = 0$. For real γ the solution [Eq. (23a)] is

$$a(t) = a(t_0) \exp\{-[\Gamma - i(\omega_0 - \Omega)](t - t_0) + i(\gamma/2\Gamma)|a(t_0)|^2(1 - e^{-2\Gamma(t-t_0)})\}. \quad (27)$$

In accordance with Eq. (11b) for delta-function pulses [$G(\xi) \rightarrow 1$], we set

$$a_{\Delta i} \equiv -\beta[\epsilon_0/\epsilon/(1+K^2)] \cos\theta A_i; \quad i = 1, 2 \quad (28)$$

to be the amplitude of the excitation caused by the i th pulse, where $A_i = E_i \Delta_i$ is the pulse area in the limit $\Delta_i \rightarrow 0$. The solution for $t > \tau$ for a two-pulse sequence is

and using

$$e^{i\eta \cos\Phi} = J_0(\eta) + 2 \sum_{m=1}^{\infty} i^m J_m(\eta) \cos m\Phi, \quad (30d)$$

where $J_m(\eta)$ is the m th order Bessel function of the first kind, we find on insertion of Eq. (29) into Eq. (16) that $V(t)$ is zero except near $t = m\tau$ ($m = 2, 3, 4, \dots$). The expression for the voltage corresponding to the echo at $t = m\tau$ is

tremes. On the other hand, in the large-signal limit the decay of the echo as a function of pulse separation τ is significantly different for the two extremes. In particular, for a single orientation θ_0 the echo amplitude oscillates as a function of τ due to the nature of the Bessel functions in Eq. (31). The period of the oscillations decreases with increasing η . For a uniform distribution of θ , the integral over θ smoothes out the oscillations either partially or completely depending on the amplitudes A_1 and A_2 . Thus we conclude that in discussing experiments on randomly oriented particles carried out in the large-signal limit the integral over θ cannot be ignored in this or any other anharmonic-oscillator theory.

The shape of the echo is determined by the re-

maining integral over ω which is dominated by the narrower of the mode distribution function $G_\omega(\omega)$ or the receiver response function $G_R(\omega)$. In the present powder experiments $G_\omega(\omega)$ can be taken to be constant and the echo shape is simply the Fourier transform of $G_R(\omega)$ when using δ -function pulses.

We note that the $m\pi$ two-pulse echoes with $m > 2$ arise quite naturally out of the anharmonic-oscillator theory with a simple fourth-order anharmonicity. This contrasts with certain types of parametric field-mode interaction theories (see Appendix).

Expanding $V_{m\tau}$ to lowest order in η we find

$$V_{m\tau} \propto i^m c_4^{m-1} A_1^{m-1} A_2^m e^{-2\Gamma(t-\tau)} (1 - e^{-2\Gamma(t-\tau)})^{m-1}. \quad (32)$$

Note that for $2\Gamma(t-\tau) \gg 1$ the $m\tau$ echoes all decay as $\exp[-2\Gamma(t-\tau)]$ where $t = m\tau$. This general behavior will be compared to experiment in Sec. IV. Note that the relative phase of $V_{m\tau}$ is given simply by the i^m factor.

Carrying out the above procedure for a three-pulse sequence readily reveals that three-pulse echoes shall occur at $t = nT + p\tau$ with $n, p = 0, \pm 1, \pm 2, \dots$ and $t > T$.

3. Finite pulse widths—Large-signal behavior

The complete evaluation of the anharmonic-oscillator model for fourth-order anharmonicity requires the numerical integration of Eq. (22a) for a two-pulse sequence and the numerical integrations over the frequency difference ω and the orientation θ in Eq. (16). This complete solution is beyond the scope of the present paper.

An approximation to the exact solution can be obtained in the following manner. Assume short but finite width pulses so that the nonlinear term ($-i\gamma|a|^2a$) in Eq. (22a) can be neglected during the applied pulses. Thus the solution during the pulses is just that given by Eq. (11). Between and after the applied pulses the exact solution to Eq. (22a) is given by Eq. (23a). Matching these solutions at the leading and trailing edges of the pulses gives the solution with the approximation that the nonlinearity is "turned off" during the pulses. This procedure has been carried out and presented elsewhere.⁶¹ The decay curves (e_2 vs τ) and the echo shapes calculated in this way show many features similar to the experimental data presented in Sec. IV. However, several inconsistencies remain and it is not yet known whether or not they can be resolved by taking account of the distribution of θ and of $\Gamma \equiv T_2^{-1}$.

III. EXPERIMENTAL METHOD

The experiments reported in this paper were performed in two frequency regimes: (a) VHF

(10–300 MHz); and (b) the C (5 GHz), X (10 GHz), and Ku (18 GHz) microwave bands. We discuss these two regimes separately.

A. VHF

The preparation of powder samples for use at VHF frequencies consisted of several steps. Single crystals were ground in a mortar and pestle and the particles sized using standard mesh screens. Then the particles were washed, so as to detach very fine particles electrostatically adhered to the larger ones and sieved once again. In most cases they were then outgassed at $\sim 200^\circ\text{C}$ and sealed in a high vacuum in a pyrex holder in which plane parallel electrodes were constructed. The electrodes were separated typically by 1 mm. In the case of GaAs we found that by briefly etching the particles prior to the final sieving, the decay constant $T_2 = \Gamma^{-1}$ could be increased by some two orders of magnitude or more. We believe that before the etching, T_2 was limited by surface damage incurred during the grinding process. The increase in T_2 achieved in this way was an important factor in the success of the experiments performed on GaAs powder. The T_2 of the quartz powder samples obtained from powdered silica (Fisher Scientific S-153) was unaffected by either etching or annealing procedures. In spite of these preparation procedures it should be noted that the individual particles of a powder sample have a very irregular shape, and consequently, extremely complex electromechanical mode structure.

A typical sample consisted of about 10^6 particles. In general it was the echo to ringing ratio which limited the accuracy of the experiments rather than the echo-to-receiver noise ratio. The echo to ringing ratio increased with increased number of particles. For fewer than 10^3 particles echoes were not detected.

A block diagram of the apparatus used at VHF frequencies is shown in Fig. 5. The rf pulses were derived from two rf pulsed oscillators (Matec 6600) whose relative pulse amplitudes, frequencies, widths, and timing were independently adjustable. Typically, the pulse amplitudes were adjustable up to 1000-V peak across the 1-mm thick samples. The pulse widths ranged between 0.5 and 16 μs and the pulse repetition rate ranged up to 1000 Hz. In most experiments the sample capacitance was resonated with a lumped series inductance or with stub tuners. The resulting bandwidths were typically 4 MHz. A boxcar integrator was used to obtain the detailed shapes of the echoes.

If an oscillator is started at $t = t_0$, the pulse is represented by the real part of Eq. (10). The relative rf phase of two pulses started at $t_0 = 0$ and

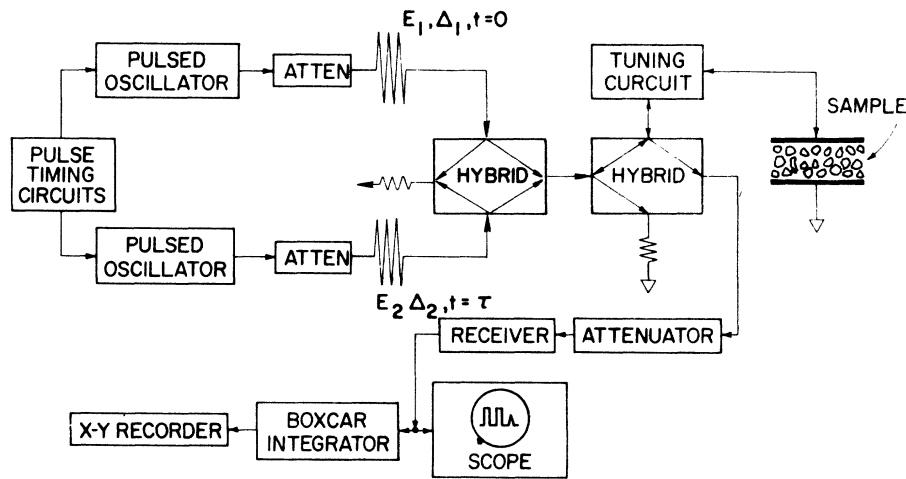


FIG. 5. A simplified block diagram of the VHF spectrometer used in the present experiments. The amplitudes E_1 and E_2 , and the widths Δ_1 and Δ_2 of the two pulses are independently variable. Additional pulses with amplitudes equal either to E_1 or E_2 could also be applied to the powder sample. The tuning circuit consisted of either a lumped series inductance or a stub tuner to resonate the sample capacitance.

at $t_0 = \tau$ is just $\omega_0 \tau$. If τ varies randomly $\delta\tau$ from one two-pulse sequence to the next, the change in phase is $\omega_0 \delta\tau$. If $\omega_0 \delta\tau \ll 1$, the pulse sequences are effectively phase coherent. If $\omega_0 \delta\tau \geq 1$, they are incoherent. In the experiments reported here the pulses were intentionally made incoherent. This insures that "static" echoes, which are generally weaker than dynamic echoes but which, when summed or integrated through the use of coherent pulse sequences, are often larger than dynamic echoes, are reduced to at least 20 dB below the dynamic echoes. Consequently, "static" echoes can be neglected in this paper.

B. X and Ku bands

All of the reported results were obtained on Fisher Z-52 ZnO powder. The particle sizes were less than 1μ as shown in Fig. 6. Experi-

ments on N.J.Zinc-HC-016-100 ZnO powder were unsuccessful, possibly because of the larger particle dimensions as seen in Fig. 7. The powder was placed in 2-mm-i.d. fused quartz tubes for use in a reentrant cavity, or, alternatively, in thin-wall pyrex boxes, approximately 1 in. in length, with the other dimensions made to provide a sliding fit inside an X-band waveguide (10 mm \times 22 mm). The containers were then pumped out and sealed at high vacuum. The effective volume of the reentrant cavity (2-mm gap) thus contained about 10^{10} particles, while the waveguide boxes held about 10^{12} particles. Ringing signals could be detected at the highest input powers used and with full receiver gain, but under the conditions at which most echo measurements were made, ringing was not observable.

Because of the larger number of powder particles, the signals observed from waveguide sam-

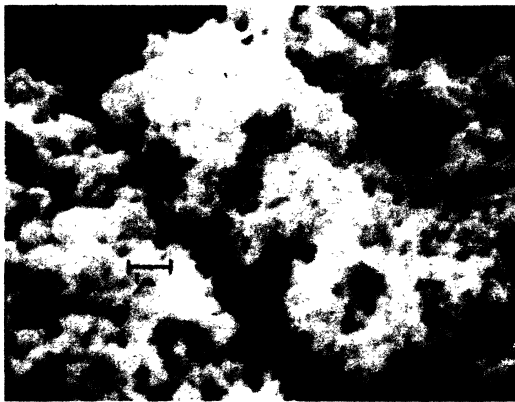


FIG. 6. Electron micrograph of ZnO powder utilized in X-Ku band-echo measurements.

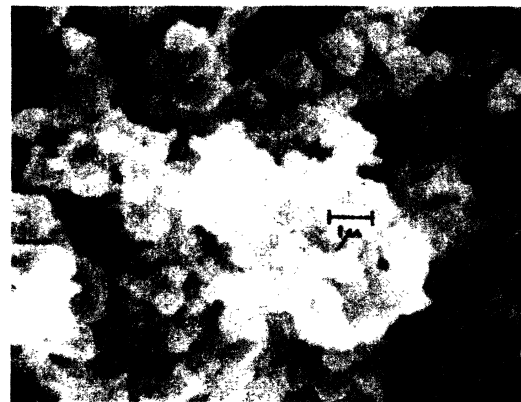


FIG. 7. Electron micrograph of a ZnO powder which did not show echoes at X-Ku band frequencies.

ples had about the same signal-to-noise ratio as those which utilized a cavity resonator, even though the latter are enhanced by the Q factor. Therefore, because of the relative convenience, as well as the increased band width which minimizes circuit distortion of echo shapes when using short pulses, all of the quantitative measurements were made on waveguide samples. However, under similar conditions of pulse amplitude and width it was determined that qualitatively similar behavior was obtained on cavity samples.

The field in a waveguide is inhomogeneous, varying sinusoidally along the direction of propagation as well as across the larger perpendicular dimension in the TE_{01} mode. The powder particles, therefore, see a distribution of fields varying from zero to a maximum value which we estimate to be about 350 V/cm at 1-kW input power. In calculating this value we have assumed the sample container to be uniformly filled with ZnO. The effect of considering empty spaces between particles could be to increase the above value by as much as 40%.

A schematic diagram of the electronic apparatus is shown in Fig. 8. The output of a tunable, frequency stabilized, cw klystron oscillator is amplified by a 10-W travelling wave tube amplifier. The output cw power is then split into three approximately equal lines, each of which contains its own attenuators and fast switches. One line also has a phase shifter. These lines can then be switched into a gated 1 kW, 32 dB gain, traveling wave tube amplifier (TWTA). The TWTA gating pulses overlap the switch pulses which have a turn on/off time < 10 ns. For all the measurements reported here, pulse widths in the range 20–300 ns were used. The output of this amplifier is then fed through a variable waveguide, precision

attenuator, and circulator into the cavity resonator or shorted waveguide which holds the samples. The latter are contained in a temperature-variable dewar. The working volume lies within the gap of a 6-in. Varian magnet, the purpose of which is to ascertain that the echo signals are not affected by magnetic fields. No magnetic effects were found up to 6 kOe.

The reflected pulses and emitted echo signals at the third part of the circulator are amplified by a low-noise TWTA and detected in a superheterodyne receiver with variable i.f. attenuation. The low-noise TWTA is not a necessity but its use obviates the need for a crystal protector before the mixer and thus allows measurements to be made at times as short as 20 ns following a high-power reflected input pulse, which would otherwise saturate the protector-mixer combination.

The overall frequency tuning range of the system is 8–18 GHz. The detection band width is 120 MHz. Since all three pulses are derived from a single cw source they are phase coherent, and this allowed echo phase measurements to be made by adding to the mixer input a small cw reference signal (obtained from the klystron output before the first TWTA) having variable phase and amplitude.

It was found early that input pulses at high repetition rates caused the sample temperature to rise significantly above the ambient, even when the containers were immersed in superfluid He. In most experiments a repetition rate of 1 per min (i.e., one input pulse pair per min) was necessary to avoid temperature-dependent variations in echo behavior. Therefore all the data were obtained on oscilloscope photographs. The photographs shown in Sec. IV are typical; each echo seen there is the result of one pair of input pulses, rather than a superposition of many. There was thus some scatter in the data, particularly at very low input powers with small-echo signal-to-noise ratios. The use of single shot data also avoids interference from storage echoes which, because the pulses are phase coherent, can occur at high-input powers. However, we have never observed storage under these conditions. All detectable storage-echoes result from integration of many pulse pairs.

Measurements of echo amplitudes were obtained directly from the scope photos and corrected for detector nonlinearity. All quoted values of T_2 were measured from echo decay envelopes at values of τ no smaller than T_2 beyond the last envelope maximum. Quoted values of e_{20} were obtained by extrapolating these measurements to $\tau=0$, along the exponential curve $e_2 = e_{20} \exp(-2\tau/T_2)$. Since $e_2(\tau=0) \equiv 0$ for powder echoes (see Sec. III), e_{20} is only a measure of the echo amplitude with the damping

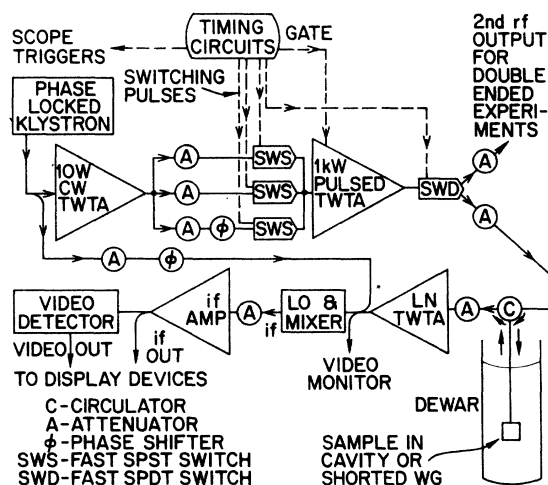


FIG. 8. Block diagram of X-Ku band-echo spectrometer.

factor removed and is thus a measure of the non-linearity, albeit only in the region of τ over which T_2 is measured.

IV. EXPERIMENTAL RESULTS-VHF

We present here the results of an extensive experimental investigation of the dynamic polarization echo phenomenon in piezoelectric powders in the VHF range. Measurements of the piezoelectric ringing are presented and compared to theory in Sec. IV A. In Sec. IV B dynamic two-pulse echo data are presented which clearly show the transition from the small-signal to the large-signal regimes. Measurements made in the large-signal limit are presented in Sec. IV C. In Sec. IV D the behavior of the damping constant $\Gamma = T_2^{-1}$ as a function of temperature, frequency, and acoustical impedance of the surrounding medium is described.

A. Piezoelectric Ringing

A typical ringing pattern is shown in Fig. 9 for LiNbO_3 . The similarity of this pattern to the calculated patterns given in Fig. 2 of Sec. II is clear.

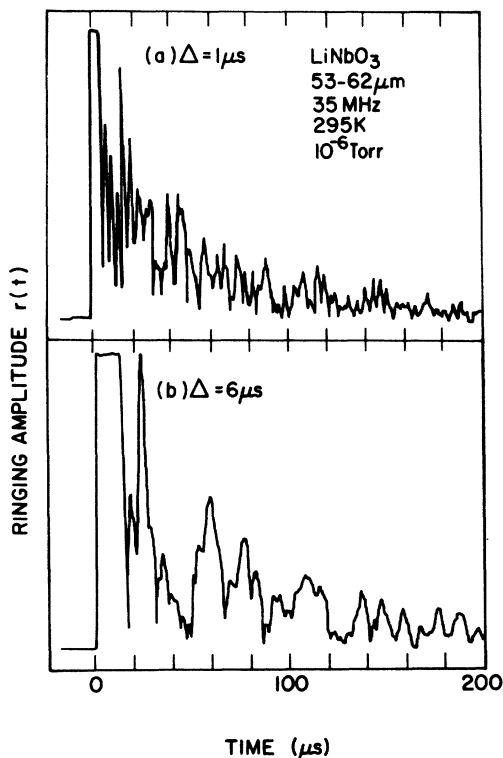


FIG. 9. Single-pulse response of a powder sample of LiNbO_3 particles 53–62 μm in diameter. The pulse widths are 1 and 6 μs for the top and bottom traces, respectively. The pulse amplitude corresponded to 250-V peak applied to the 1-mm sample.

In general, echoes are totally obscured by the ringing in samples with a small number of particles ($\leq 10^3$), whereas for large numbers of particles ($\sim 10^{12}$ in ZnO at X band) the ringing is barely detected due to phase cancellation. The decay constant Γ obtained from the ringing is consistent with that obtained from the two-pulse echo decay. This is consistent with the calculations in Sec. II, where the decay constant for both the ringing and the two-pulse echo arise from the damping of the mechanical oscillations of the individual particles.

The frequency dependence of the ringing amplitude r (corrected for frequency dependence of Γ) is shown in Fig. 10 for LiNbO_3 powder. The low-frequency cutoff frequency is given by $\nu_c \sim v/4b$, where b is the radius of the largest particles of the sample and v the effective sound velocity. This is consistent with the decrease in ν_c for larger particles as shown in Fig. 10. Because of the many higher-frequency modes of a particle which can contribute to the ringing (and the echoes), there is no sharp high-frequency cutoff. In fact, as shown in Fig. 10, there is only a slow decrease of r with increasing frequency although the particle size distributions are fairly narrow.

The ringing amplitude as given by Eqs. (11)–(14) is clearly expected to be linear in the applied pulse amplitude. The measurements shown in Fig. 11 for GaAs powder are clearly in good agreement with this prediction based upon the linear theory.

The dependence of the ringing amplitude on pulse width is shown in Fig. 12 for GaAs powder and can be compared to the theoretical result in Fig. 3. The dependence on pulse width is not linear because the width determines not only the am-

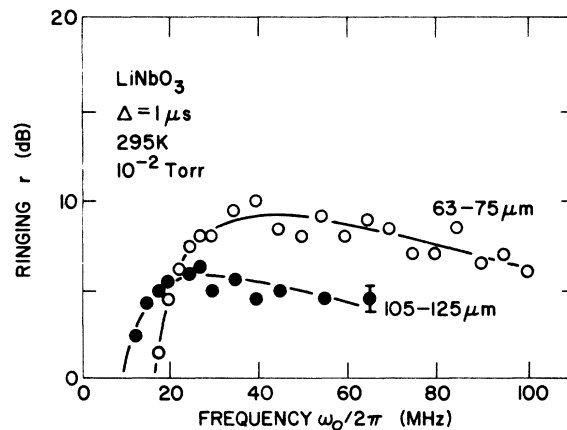


FIG. 10. Frequency dependence of the ringing amplitude in LiNbO_3 powders of different sizes. The data have been corrected for differences in the decay time T_2 . Pulse amplitude corresponded to 250-V peak across 1-mm sample.

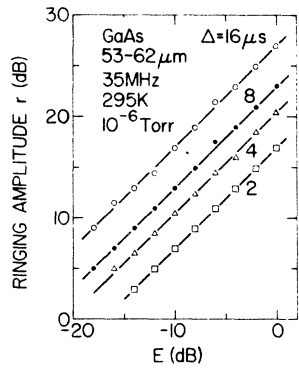


FIG. 11. Ringing amplitude r in dB vs the applied pulse amplitude E , also in dB in GaAs. Data for pulse widths of 16, 8, 4, 2 μ s are shown. The straight lines correspond to a slope of one.

plitude of particle excitation as given by Eq. (11b), but also the Fourier spectrum of the pulse as given by Eq. (11c).

We believe that these data show that the ringing signal detected after a single applied pulse can be easily understood as being simply the partially phase-cancelled radiation of the finite number of individual piezoelectric particles. Therefore, the ringing is not related to the free-induction decay of a spin system.³⁴

B. Transition to Large-signal limit

In the small-signal limit the predictions of the anharmonic-oscillator model are unambiguous and are described in Sec. II C 1. In the large-signal limit the predictions of the anharmonic-oscillator model become model dependent. For δ -function pulses the results for a special case are discussed in Sec. II C 2. We present here data which are in good agreement with the small-signal theory, at the lowest rf powers attainable consistent with a reasonable signal to noise. However, at higher

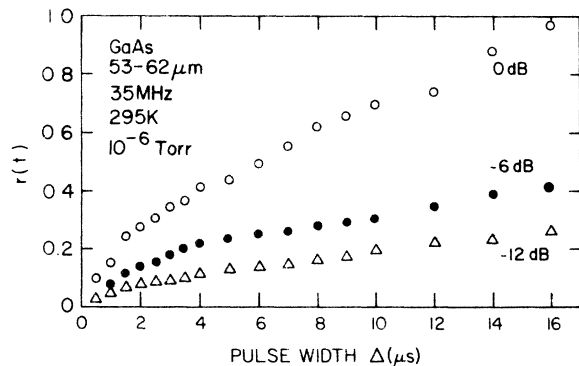


FIG. 12. Ringing amplitude r (arbitrary units) vs pulse width for different pulse amplitudes in GaAs powder. 0 dB correspond to 800-V peak across 1-mm sample.

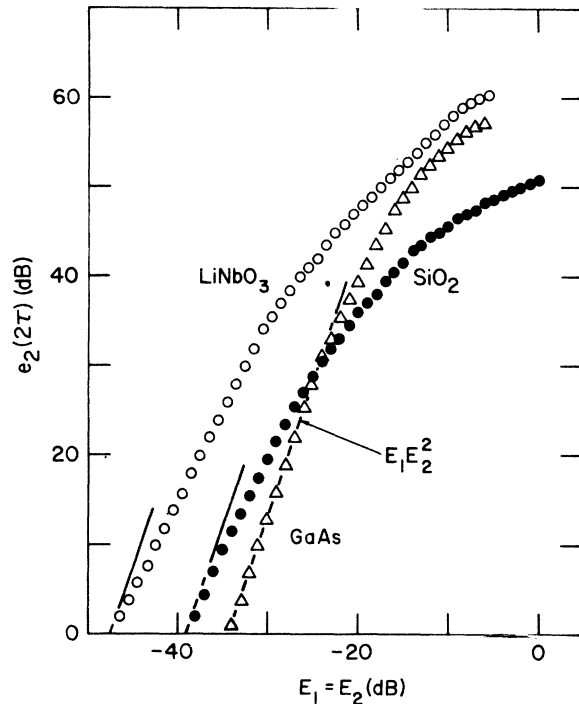


FIG. 13. Dependence of two-pulse echo amplitude $e_2(2\tau)$ on pulse amplitude with $E_1 = E_2$. The straight lines correspond to a slope of 3. Data for LiNbO_3 , GaAs, and SiO_2 powder at $\omega_p/2\pi \sim 35$ MHz are shown.

powers, significant deviations from the theory are found which indicate the onset of large-signal behavior. In the absence, as yet, of complete large-signal calculations no quantitative comparison with experiment in the large-signal regime will be made.

On the basis of Eq. (25), when $E_1 = E_2 \equiv E$ the echo amplitude should vary as the third power of the applied field amplitude E . In Fig. 13 we show the power dependence obtained in LiNbO_3 , SiO_2 , and GaAs. Clearly, only in GaAs at the lowest attainable power level is the expected E^3 behavior found. Thus, consistent with the results described below, only in GaAs at very low powers is the small-signal limit valid. In all other experiments described in this paper the small-signal limit is invalid.

The decay of the two-pulse echo amplitude $e_2(2\tau)$ with pulse separation τ is shown for GaAs in Fig. 14. Also shown (dashed curve) is the expected small-signal behavior from Eq. (25) fit to agree with experiment at the maximum in the echo amplitude. As expected from the anharmonic-oscillator theory and clearly shown in the data, the echo amplitude builds up from zero at $\tau = 0$ to a maximum before decaying exponentially for large τ . However, the agreement is not perfect. In general the data build up faster and/or decay slow-

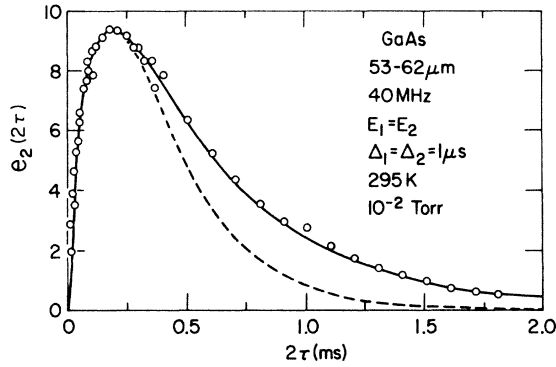


FIG. 14. Dependence of two-pulse echo amplitude $e_2(2\tau)$ on twice the pulse separation 2τ in GaAs powder. The scale of the ordinate is arbitrary. Pulse amplitudes correspond to 620-V peak across the 1-mm sample. The dashed curve corresponds to Eq. (25) fitted at the maximum by varying $\Gamma \equiv T_2^{-1}$. The solid curve is obtained by assuming a Maxwellian distribution of Γ 's as described in the text.

er than the theory predicts if a single value of the decay constant Γ is assumed to characterize the powder sample. Assuming a Maxwellian distribution of Γ 's of the form

$$G_{\Gamma}(\Gamma) = \left(\frac{\Gamma - \Gamma_c}{\Gamma_0} \right)^2 \exp \left[-\frac{1}{2} \left(\frac{\Gamma - \Gamma_c}{\Gamma_0} \right)^2 \right], \quad (33)$$

and fitting it to the data, the solid curve in Fig. 14 is readily obtained for $\Gamma_0 = 2.1 \times 10^3 \text{ s}^{-1}$ and $\Gamma_c = 0.42 \times 10^3 \text{ s}^{-1}$. As equally good fit to the data can be obtained by a careful choice of just two equally weighted values of Γ . Although care must clearly be taken in interpreting the fit of the solid curve and the data in Fig. 14, the underlying assumption that the powder sample is characterized by more than one value of Γ is not unexpected physically. There is no reason to believe that the many different types of modes contributing to the echo have the same Γ . For small τ the modes with the largest Γ dominate giving a fast build up of $e_2(2\tau)$. For large τ the modes with small Γ dominate. Thus the decay behavior for large τ is a measure of the Γ of the modes which are least damped. The presumed distribution of Γ 's in a given powder sample is yet another complication when attempting to fit calculations in the large-signal limit to experiment.

The decay behavior in GaAs and LiNbO₃ as a function of applied pulse amplitude is shown in Fig. 15. In GaAs the only effect of increasing the pulse amplitude is an apparent slight decrease in Γ as determined from the decay at large τ . In LiNbO₃ the decay is much more sensitive to amplitude. At low amplitude the decay is qualitatively similar to the small-signal theory. At higher am-

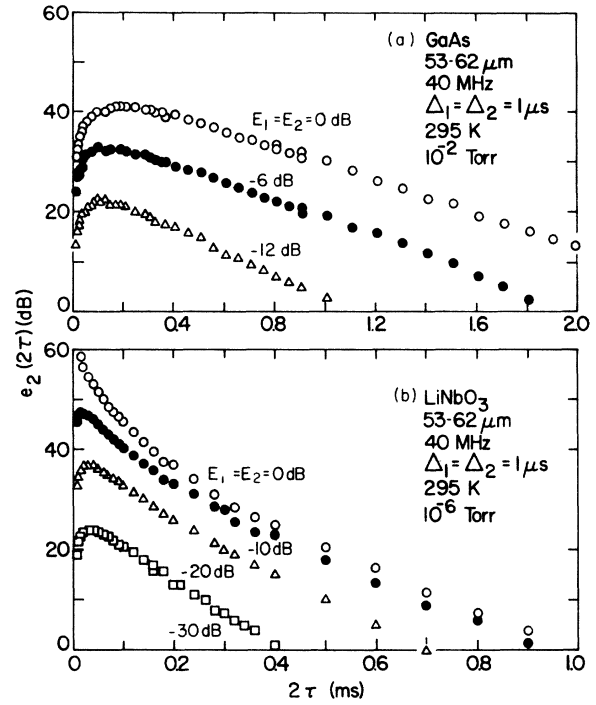


FIG. 15. The decay behavior of $e_2(2\tau)$ as a function of twice the pulse separation 2τ in GaAs (a) and LiNbO₃ (b). The different curves correspond to different rf pulse amplitudes. Both pulses had equal amplitudes and widths. In (a) and (b) 0 dB corresponds, respectively, to 620 and 500-V peak across 1-mm samples.

plitudes the position of the maximum moves to smaller pulse separation τ until at the highest amplitudes attainable the maximum is no longer detected since it occurs during the receiver dead time following the second pulse. The interpretation of these data is that as the small-signal limit is exceeded the buildup occurs more and more rapidly owing to the increased nonlinearity of the process. Consequently, the maximum occurs at smaller pulse separation. This behavior is confirmed by computations based upon the results for the δ -function model presented in Sec. II C 2.

In the small-signal limit typical echo shapes expected on the basis of the anharmonic-oscillator model were given in Fig. 4. The experimental shapes for GaAs as a function of pulse amplitude and pulse separation are given in Figs. 16 and 17, respectively. For equal pulse widths ($\Delta_1 = \Delta_2 = \Delta = 6 \mu\text{s}$) and amplitudes the two bottom traces in Fig. 16 at the lowest powers have the expected base width of $\Delta_1 + 2\Delta_2 = 3\Delta$. At higher powers the shape changes continuously becoming almost rectangular in shape with small side lobes, the base of the rectangle being approximately equal to a single-pulse width. The data shown in Fig. 17 in-

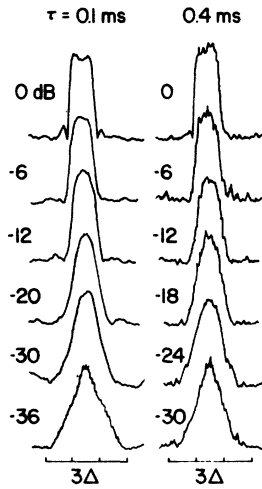


FIG. 16. Two-pulse echo shapes in GaAs powder (53–62 μm) at two different pulse separations τ and at several different pulse amplitudes indicated in dB on the figure. The pulse amplitudes and widths ($\Delta_1 = \Delta_2 = \Delta = 6 \mu\text{s}$) were equal. Data taken at 295 K in a vacuum of 10^{-6} Torr. 0 dB corresponds to 1000 V across the 1-mm thick powder sample.

dicates that the echo shapes are in general dependent upon the pulse separation τ . For very large τ the shapes are those expected in the small-signal limit, whereas for small τ (but not $\Gamma\tau \ll 1$) the shapes become similar to the large-amplitude shapes shown in Fig. 16. The τ dependence of the echo shapes confirms the validity of the small-

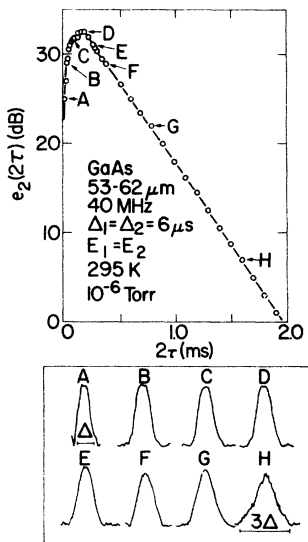


FIG. 17. Two-pulse echo-decay behavior and the echo shapes in GaAs powder at different points on the decay curve. The pulse widths were equal ($\Delta_1 = \Delta_2 = 6 \mu\text{s}$) as were the amplitudes which corresponded to 70-V peak across the 1-mm sample.

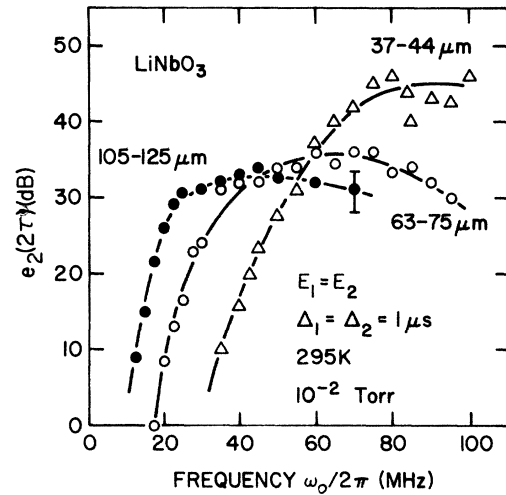


FIG. 18. Frequency dependence of two-pulse echo amplitude $e_2(2\tau)$ in LiNbO₃ powder for three different size distributions as indicated. The data have been corrected for changes in the decay time T_2 . Pulse amplitude corresponds to 250-V peak across 1-mm sample.

signal approximation as $\Gamma\tau \gg 1$ in agreement with Eqs. (26) and (30a) above.

The frequency dependence of the echo amplitude in LiNbO₃ is indicated in Fig. 18 for three different particle sizes. The indicated behavior is similar to that for the ringing amplitude shown in Fig. 10. Because of the uncertain mode distribution for the powder samples, a detailed analysis of the data does not seem warranted. However, shown clearly in Fig. 18 is the decrease in the low-frequency cutoff with increasing particle size as expected.

The dependence of the echo amplitude on temperature can shed some light on the source of the anharmonicity. The temperature dependence of the echo amplitude $e_2(2\tau)$ (corrected for the temperature dependence of Γ) for GaAs, LiNbO₃, and SiO₂ are shown in Fig. 19. Over the range $4.2 < T < 375$ K the maximum change in $e_2(2\tau)$ is about 10

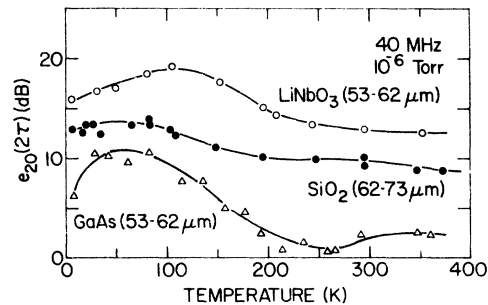


FIG. 19. Temperature dependence of the echo amplitude $e_2(2\tau)$ in LiNbO₃, SiO₂, and GaAs powder. The data have been corrected for changes in T_2 .

dB. This contrasts with the T^{-1} dependence reported in Ref. 30. The weak dependence reported here may well be an experimental artifact related to the "settling" of the powder in the sample holder, changes in T_2 , and/or large-signal effects. We believe that the small variation with temperature which can be deduced from Fig. 19 can be assumed to arise from the anharmonic coefficient itself and has nothing to do with the thermal population of quantum energy levels or defect states. The dynamic echo process in the powder considered here is essentially independent of temperature in the VHF range.

In concluding this subsection we note the following: (i) the small-signal behavior is only rarely obtained in these experiments. At the most commonly used pulse amplitudes (fields greater than 10^3 V/cm) large-signal effects are clearly visible in the power dependence, decay behavior, and echo shapes. (ii) In those cases in which small-signal behavior is attained the data is clearly in agreement with the anharmonic-oscillator model and not the parametric field-mode interaction. (iii) The frequency dependence is consistent with the excitation of mechanical modes of the individual particles. (iv) The weak-temperature dependence is consistent with some form of lattice anharmonicity and certainly does not correspond to any sort of Curielike susceptibility.³⁰

C. Large-signal behavior

As discussed above, except in GaAs at the lowest amplitudes consistent with adequate signal to noise, the experimental data are not consistent with the small-signal approximation. In this subsection we present representative data taken in the large-signal limit. Although apparently quite complex these data are internally consistent and representative of the large-signal behavior. A complete large-signal theory must be capable of describing both the echo shapes and the echo decay behavior presented here.

In Fig. 20 the dependence of $e_2(2\tau)$ on the first-pulse amplitude E_1 is shown for several values of the second-pulse amplitude E_2 in GaAs, LiNbO₃, and SiO₂. Since narrow pulses ($\Delta_1 = \Delta_2 = 1 \mu\text{s}$) were used, distortions of the echo shape with amplitude were unimportant. In all cases $e_2(2\tau)$ is proportional to E_1 as long as $E_1 < E_2$. For $E_1 \geq E_2$, $e_2(2\tau)$ exhibits a maximum before decreasing slowly with increasing E_1 for $E_1 > E_2$. In Fig. 21 the dependence upon the second-pulse amplitude E_2 for different E_1 is shown. For $E_2 < E_1$, $e_2(2\tau) \propto E_2^2$, whereas for $E_2 > E_1$, $e_2(2\tau)$ is relatively independent of E_2 . Although the small-signal limit [Eq. (25)] yields $e_2(2\tau) \propto E_1 E_2^2$, it does not suggest the

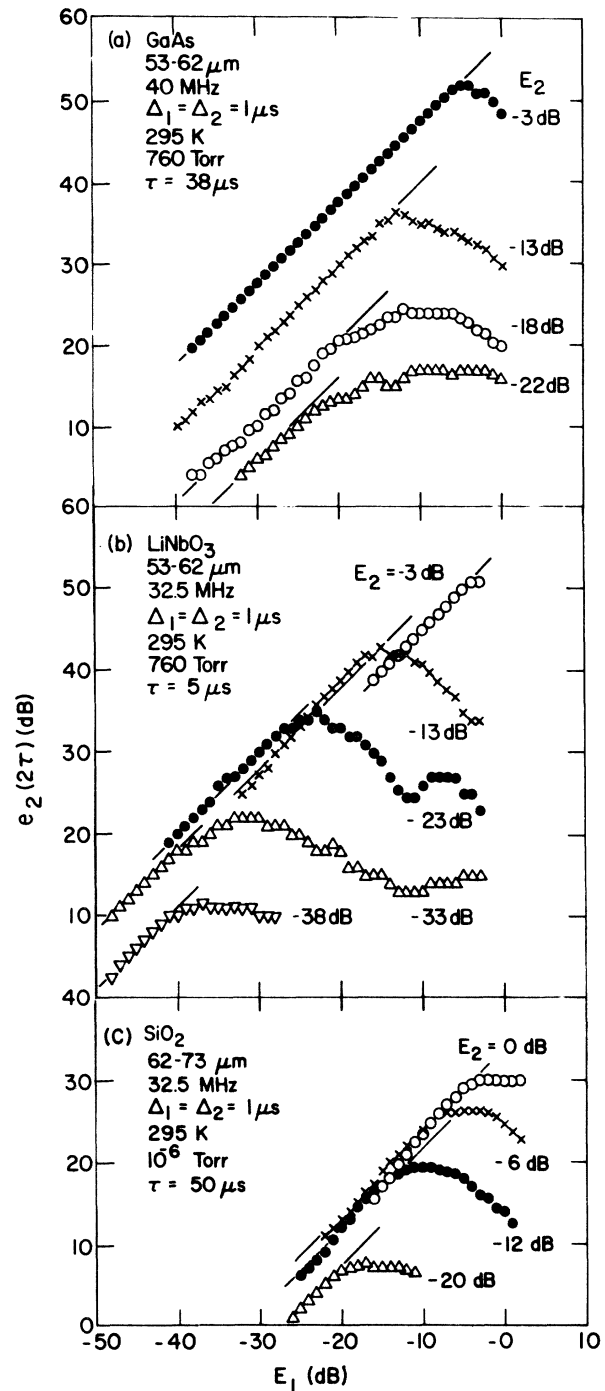


FIG. 20. Two-pulse echo amplitude $e_2(2\tau)$ vs amplitude E_1 of the first pulse for several values of the second-pulse amplitude E_2 : (a) GaAs; (b) LiNbO₃; (c) SiO₂.

interdependence of E_1 and E_2 as indicated in Figs. 20 and 21. This interdependence can only be explained by a theory valid for large signals.

The data in Fig. 22 show the decay behavior of the two-pulse echo in SiO₂ as a function of pulse

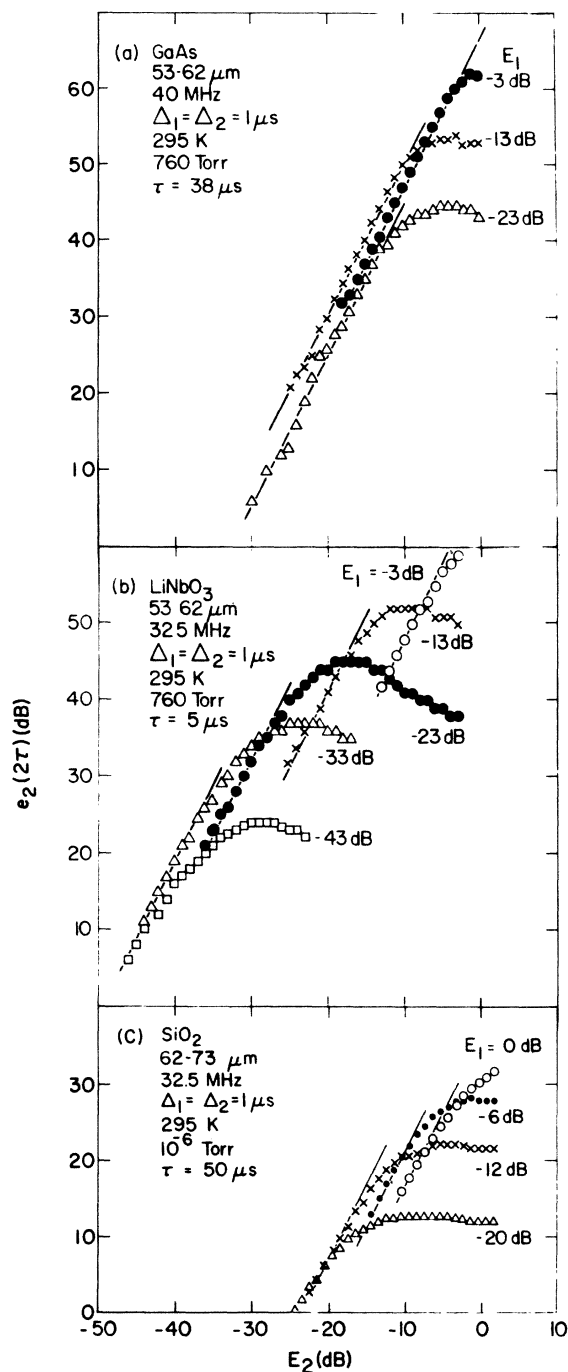


FIG. 21. Two-pulse echo amplitude $e_2(2\tau)$ vs amplitude E_2 of the second pulse for several values of the first-pulse amplitude E_1 : (a) GaAs; (b) LiNbO₃; (c) SiO₂.

amplitude for two identical input pulses of amplitudes $E_1 = E_2$ and widths $\Delta_1 = \Delta_2 = 6 \mu\text{s}$. At the lowest power (-20 dB) the simple buildup and decay as discussed in Sec. IV B is seen. At the highest power (0 dB) only the decrease in $e_2(2\tau)$ for in-

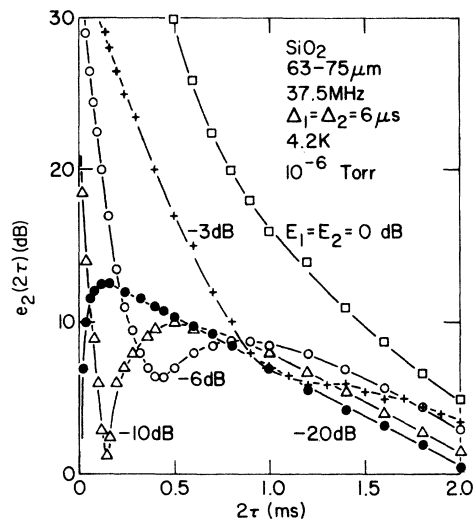


FIG. 22. Decay of two-pulse echo $e_2(2\tau)$ vs twice the pulse separation 2τ in SiO₂ powder. Different curves correspond to different pulse amplitudes as indicated with $E_1 = E_2$ and $\Delta_1 = \Delta_2 = 6 \mu\text{s}$. (0 dB corresponds to 800-V peak across the 1-mm sample.) The echo amplitude was measured at the center of the echo.

creasing τ is detected. At intermediate power levels (-3, -6, and -10 dB) the amplitude initially decreases reaching a minimum and then increases to a maximum before decaying for large τ . Any buildup of the echo amplitude from zero for $\tau = 0$ is obscured by the receiver dead time. The amplitude is measured at the center of the detected echo. In the region of the minimum, the echo shape is quite complex as discussed below.

Decay curves taken with constant value of the first-pulse amplitude E_1 , but with three different values of E_2 corresponding to $E_2 = E_1$, E_2 5 dB below E_1 , and E_2 12 dB below E_1 , are shown in Fig. 23. Again the pulse widths Δ_1 and Δ_2 are both $6 \mu\text{s}$. Note that the depth and the position of the minimum are a function of the ratio $E_1 : E_2$; the minimum is deeper and occurs at smaller pulse separations τ as this ratio increases.

In Fig. 24 the decay behavior for a constant ratio of E_1 to E_2 (with E_1 greater than E_2 by 3 dB) are shown for different absolute amplitudes of E_1 and E_2 . The depth of the minimum is relatively unchanged for the different curves although the position of the minimum moves to smaller values of the pulse separation τ as the absolute power decreases. At sufficiently low power the data exhibit only the simple buildup and decay (not shown here).

Again in SiO₂, Fig. 25 shows the decay behavior at high power for $E_1 = E_2$, E_1 greater than E_2 by 3 dB, and E_1 less than E_2 by 3 dB. The echo shapes are also shown for several values of τ for

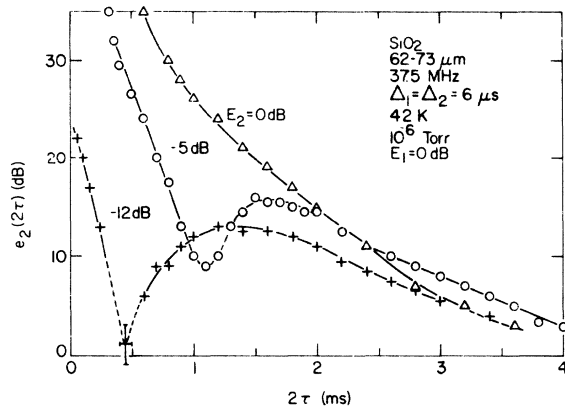


FIG. 23. Decay of two-pulse echo amplitude $e_2(2\tau)$ vs twice the pulse separation 2τ in SiO_2 powder. All data correspond to fixed first-pulse amplitude $E_1 = 0$ dB, and to fixed pulse widths $\Delta_1 = \Delta_2 = 6 \mu\text{s}$. The second-pulse amplitude is different for the three curves as indicated (0 dB corresponds to 800-V peak across the 1-mm sample). The echo amplitude is measured at the center of the echo.

each of the three curves. The striking feature of the data is that for E_1 less than or equal to E_2 the data show a simple decay with relatively little structure to the echo shape (especially for $E_1 < E_2$). However for $E_1 > E_2$ the echo shape shows a very complicated τ -dependent structure and the echo amplitude measured at the center of the echo shows the sharp minimum described above. This property, that the structure in the shape of the echo and the minimum in the decay curve are most pronounced for any given power level when $E_1 > E_2$, is a general result in all our experiments at high power. We believe that this fact may provide a

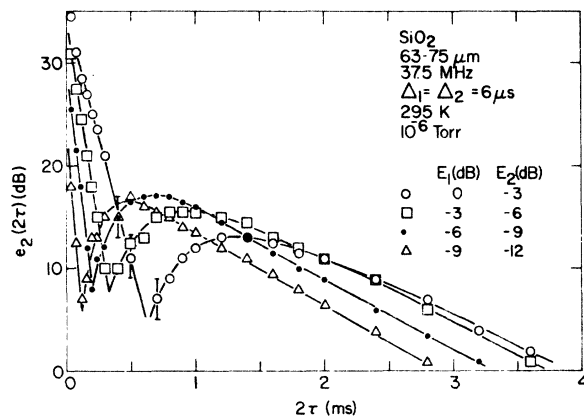


FIG. 24. Decay of two-pulse echo amplitude $e_2(2\tau)$ vs twice the pulse separation 2τ in SiO_2 powder. All data with $\Delta_1 = \Delta_2 = 6 \mu\text{s}$ and with the first-pulse amplitude E_1 3 dB greater than the second-pulse amplitude E_2 , as indicated for the four curves. The echo amplitude is measured at the center of the echo.

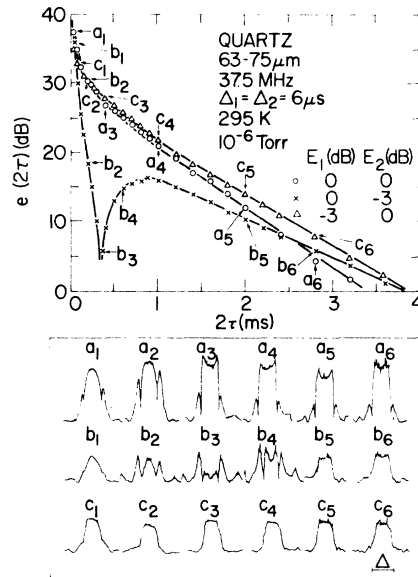


FIG. 25. Two-pulse echo amplitude $e_2(2\tau)$ and shapes vs twice the pulse separation 2τ in SiO_2 powder. All data with $\Delta_1 = \Delta_2 = 6 \mu\text{s}$ and for the values of pulse amplitudes as indicated (0 dB corresponds to 760-V peak across the 1-mm sample). The letters above the echo shapes correspond to those on the decay curves. The echo amplitude is measured at the center of the echo.

key to the understanding of the large-signal experiments.

Four typical echo shapes observed in SiO_2 at high powers are shown in Fig. 26. In each case the first-pulse amplitude E_1 is 3 dB greater than the second, E_2 . The different shapes correspond to different pulse widths Δ_1 and Δ_2 as indicated. The exceedingly structured echo shapes are typical of the large-signal behavior.⁶²

Echo shapes in GaAs for very different values of the pulse widths Δ_1 and Δ_2 at high power are shown in Fig. 27. For short pulses ($\Delta_1 = \Delta_2 = 1 \mu\text{s}$) the echo is a simple peaked structure about which little detail can be determined because of the band pass of the receiver. For both pulses wide ($\Delta_1 = \Delta_2 = 10 \mu\text{s}$) the echo has a rectangular shape whose width is equal to the pulse width $\Delta_1 = \Delta_2$. When the first pulse width Δ_1 is ten times the second pulse width Δ_2 the echo has a multiple double-peaked shape with the double peaks separated by the width Δ_1 of the first pulse. Similarly, when $\Delta_2 = 10\Delta_1$ a different multiple peaked structure is observed with the single peaks separated by Δ_2 . These shapes should be compared with the shapes shown in Fig. 4 calculated in the small signal limit. The experimental shapes shown here are observed in all materials studied under similar conditions of pulse amplitude and widths.

A related high-power coherent effect occurs when

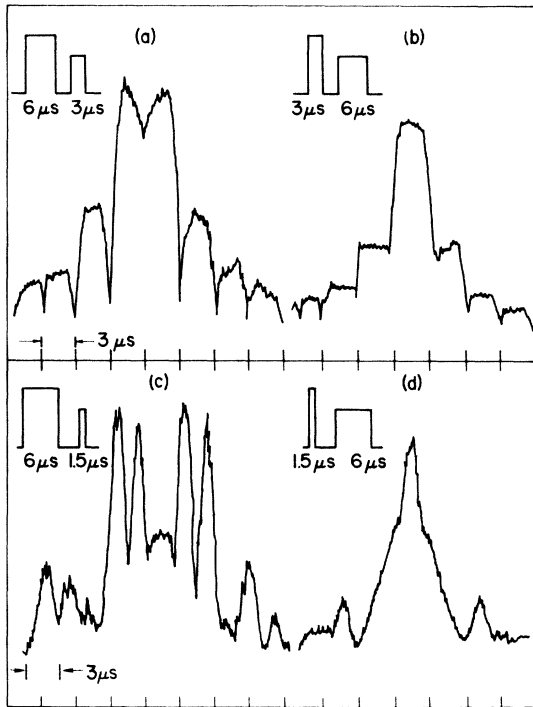


FIG. 26. Two pulse echo shapes in SiO_2 for various combinations of the pulse widths Δ_1 and Δ_2 . The first-pulse amplitude E_1 corresponds to 800-V peak across the 1-mm sample and E_2 is 3 dB less. The pulse widths are indicated by the schematic representation of the two-pulse sequence used in each case. The pulse separation τ , was 400 μs .

a single long pulse of width Δ is applied to the sample. The oscillations started by the leading part of the applied pulse interact anharmonically with those excited by later portions of the same pulse to produce a coherent "edge" echo at times spaced by the pulse width Δ . This edge echo effect is shown in Fig. 28 for $\Delta = 10$ and 20 μs . Such edge echoes were discussed by Bloom⁸³ for the case of long pulses applied to a resonant spin system. The precise relation between the edge echoes shown here and those reported by Bloom is not yet clear and awaits the evaluation of an anharmonic-oscillator theory valid for large signals with pulses of finite width. All materials we have studied exhibit edge echoes of the type described here and shown in Fig. 28.

In the large-signal limit multiple two-pulse echoes $e_2(m\tau)$ are detected at times $t = 3\tau, 4\tau, 5\tau, \dots$ in addition to the echo $e_2(2\tau)$ at $t = 2\tau$. An example of these is shown in Fig. 29 for $m = 2, 3, 4, 5,$ and 6 in GaAs. These echoes arise naturally from the anharmonic-oscillator theory as described in Sec. IIC2 explicitly in the δ -function pulse limit. These multiple echoes are

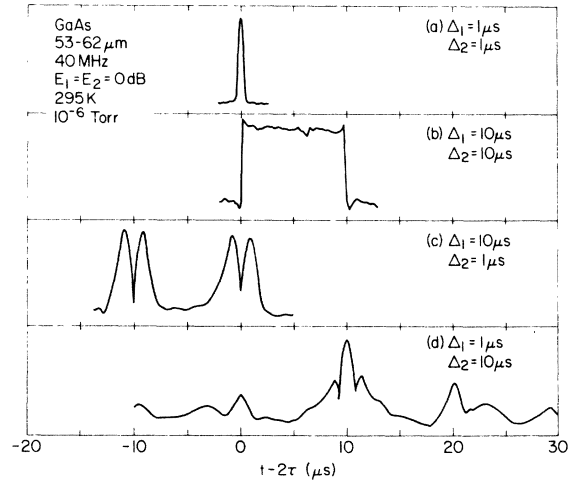


FIG. 27. Boxcar tracing of the two-pulse shapes in GaAs for $E_1 = E_2$ (corresponding to 800-V peak across the 1-mm sample) and for the pulse widths Δ_1 and Δ_2 indicated beside the four shapes. Compare to theoretical shapes in Fig. 4.

not the result of the 2τ echo acting as a pulse which together with the pulse applied at $t = \tau$ would produce the 3τ echo. This explanation, which may be valid in a spin system and has been suggested to explain the multiple echoes in piezoelectric powders,³¹ does not explain the multiple echoes in powders, as one can easily see simply from a consideration of the amplitudes of the echoes in-

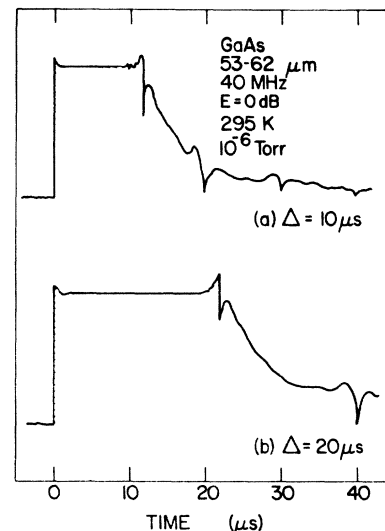


FIG. 28. Boxcar tracing of the single-pulse response for a long, high-amplitude pulse (shaded area) applied to GaAs powder. The "edge" echoes appear as sharp dips with spacing equal to the pulse width Δ . The pulse amplitude of 0 dB corresponds to 800-V peak applied across the 1-mm sample. The receiver is saturated during the applied pulse.

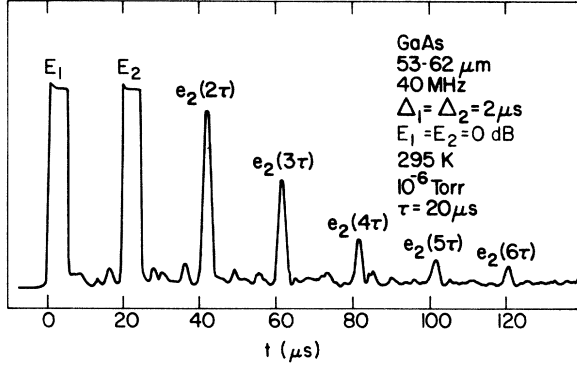


FIG. 29. Boxcar tracing of the $m\tau$ echoes ($m=2, 3, 4, 5,$ and 6) from GaAs powder with $\Delta_1=\Delta_2=2\ \mu\text{s}$, $E_1=E_2=0\ \text{dB}$ (corresponding to 800-V peak across the 1-mm sample) and with $\tau=20\ \mu\text{s}$. The two applied pulses are indicated at $t=0\ \mu\text{s}$ and $t=20\ \mu\text{s}$ (receiver saturated).

volved.

The decay behavior of the multiple echoes is shown in Fig. 30 for echoes occurring at $t=2\tau, 3\tau, 4\tau,$ and 5τ in GaAs. Note that the data is plotted as a function of $t-\tau$, where t is the time at which the echo occurs (i.e., $t=m\tau$). As expected from the large-signal δ -function analysis presented in Sec. II C 2 [Eq. (32)], the $m\tau$ echo decays as $\exp[-2\Gamma(t-\tau)]$ for $2\Gamma(t-\tau) \gg 1$, where $t=m\tau$ and Γ is the same for all m .

The pulse amplitude dependence of the 3τ echo in GaAs is shown in Fig. 31. As described earlier for the 2τ echo, there is a clear interdependence of the pulse amplitudes E_1 and E_2 . For $E_1 < E_2$,

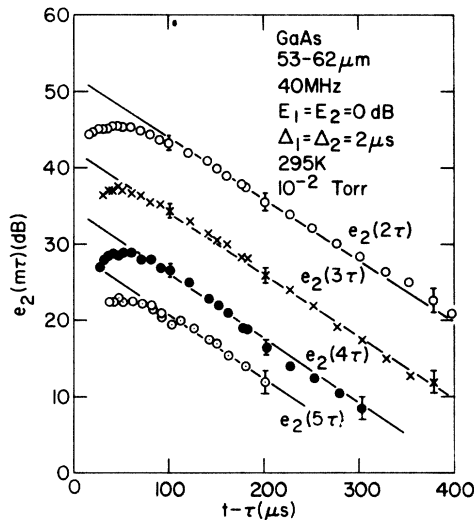


FIG. 30. Decay of the $m\tau$ echoes ($m=2, 3, 4, 5$) in GaAs powder plotted vs $t-\tau$ (where $t=m\tau$, $m=2, 3, 4, 5$). $\Delta_1=\Delta_2=2\ \mu\text{s}$, $E_1=E_2=0\ \text{dB}$ (corresponding to 800-V peak applied across the 1-mm sample).

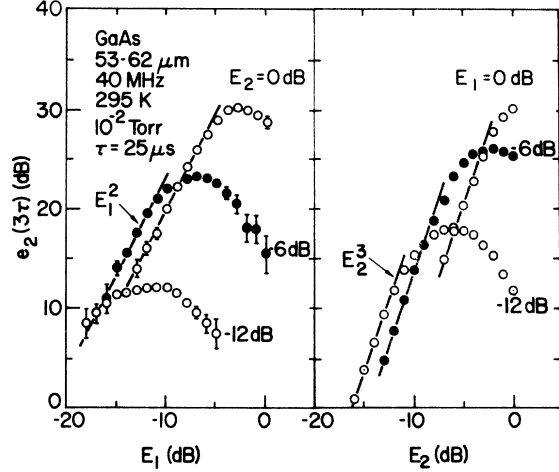


FIG. 31. Dependence of the amplitude of the 3τ two-pulse echo $e_2(3\tau)$ in GaAs on the pulse amplitudes E_1 and E_2 . The solid lines on the left and right sides correspond to slopes of 2 and 3, respectively. On the left and right sides 0 dB corresponds to 740 and 650 V across the 1-mm sample, respectively.

$e_2(3\tau) \propto E_1^2$, and for $E_2 < E_1$, $e_2(3\tau) \propto E_2^3$. The predicted small-signal behavior from Eq. (32) is $e_2(3\tau) \propto E_1^2 E_2^3$.

D. Measurement of the decay constant $\Gamma=T_2^{-1}$

The analysis presented in Sec. II has completely neglected particle-particle interactions and consequently there is assumed to be no irreversible dephasing of the particles due to such interactions. Therefore, the decay constant $\Gamma=T_2^{-1}$ of the two-pulse echo is associated with decay of the amplitude of an individual oscillator whose energy decays as 2Γ . The independent particle assumption of the models considered to date is thus equivalent to the lifetime-limited regime of conventional spin echoes ($T_2=2T_1$). To within our experimental accuracy we always find that for dynamic echoes the decay time T_1 of the three-pulse echo is equal to $\frac{1}{2}T_2$, thus confirming the validity of this conjecture. This relationship ($T_1=\frac{1}{2}T_2$) has been found previously by others.²⁰

Since the decay time $\frac{1}{2}T_2$ determines the rate of loss of energy from a given mode of an individual particle, it is of some interest to determine its origin. In the following discussion of various experimental conditions which influence T_2 we have determined T_2 from the decay of the two-pulse echo $e_2(2\tau)$ for large τ where $e_2(2\tau) \sim e^{-2\tau/T_2}$. Although this result can be rigorously justified only in the small-signal limit or, equivalently, at very large τ , we believe that these determinations of T_2 are probably valid as long as the decay of the two-pulse echo is exponential over a range in time

of at least T_2 in length.⁶⁴

A mode of oscillation can lose energy through processes internal to the particle or through processes in which energy is transmitted through the surface of the particle to the surrounding medium. In general, the internal loss mechanisms are those responsible for ultrasonic attenuation and include mode conversion, phonon scattering, interaction with crystalline defects or impurities, etc. However, one should note that the particle surface can play an important role in these internal losses. An example of the role of surfaces in determining energy loss (i.e., T_2) was given in Sec. III when we showed that careful removal of surface damage, which was incurred during grinding of GaAs into powder form, increased T_2 by some two orders of magnitude.

Immersing the particles in a gaseous medium will in general decrease the measured T_2 because of the loss of energy through the surface to the gas. This effect is shown in Fig. 32, where we plot the echo amplitude vs 2τ in GaAs for the powder immersed in several different gases. The data show quite clearly that the measured T_2 is a sensitive function of the type of gas present. The energy loss through the surface of the oscillating particle per unit time is defined by

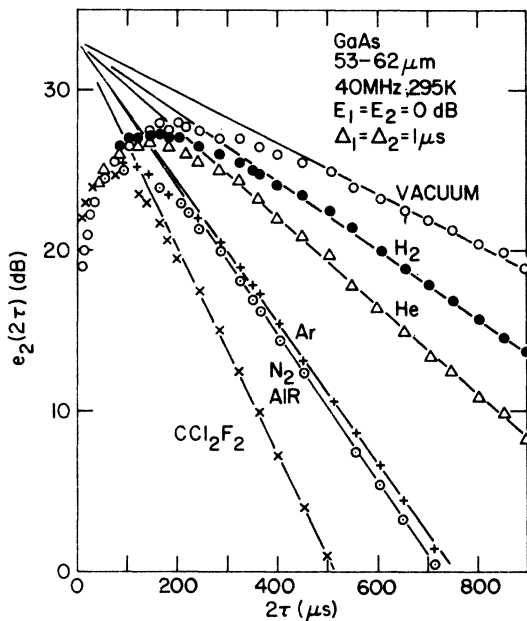


FIG. 32. Two-pulse echo $e_2(2\tau)$ decay vs twice the pulse separation 2τ in GaAs powder. The different curves correspond to the powder immersed in each of the five gases indicated at one atmosphere pressure and also in vacuum of 10^{-2} Torr. The pulse amplitudes of 0 dB correspond to 620-V peak across the 1-mm sample.

$$\frac{1}{U} \frac{\partial U}{\partial t} = -2\Gamma = -2T_2^{-1}, \quad (33)$$

where U is the energy of the mode considered. The relaxation rate T_2^{-1} can be written as the sum of an intrinsic loss term T_{2i}^{-1} and a loss term which corresponds to energy transmission through the surface to the gas T_{2g}^{-1} , so that $T_2^{-1} = T_{2i}^{-1} + T_{2g}^{-1}$. The transmission of sound through the surface is governed by the acoustical impedances Z_s and Z_g of the solid and gas, respectively. The transmission coefficient \mathcal{T} for sound passing through the surface is related to T_{2g}^{-1} through

$$2T_{2g}^{-1} = \mathcal{T} \frac{\omega_0}{2\pi} \equiv \frac{4Z_s Z_g}{(Z_s + Z_g)^2} \frac{\omega_0}{2\pi} \approx \frac{2\omega_0}{\pi} \frac{Z_g}{Z_s}; \quad (Z_s \gg Z_g). \quad (34)$$

The data in Fig. 33 show the behavior of T_2^{-1} as a function of Z_g for the gases used in Fig. 32. The linear behavior is in agreement with the above analysis. The intercept on the ordinate is a measure of the intrinsic loss rate T_{2i}^{-1} . The slope of the straight line can be used to calculate the effective acoustical impedance of the solid particle $Z_s (= \rho v)$. From Fig. 33 we find $Z_s \approx 2.3 \times 10^6$ g/cm²s for GaAs. Using⁶⁵ $\rho = 5.3$ g/cm³ this corresponds to an effective sound velocity $v \approx 4.2 \times 10^5$ cm/s. This velocity is in good agreement with the known sound velocities in GaAs.⁶⁶

The frequency dependence of T_2^{-1} over the range

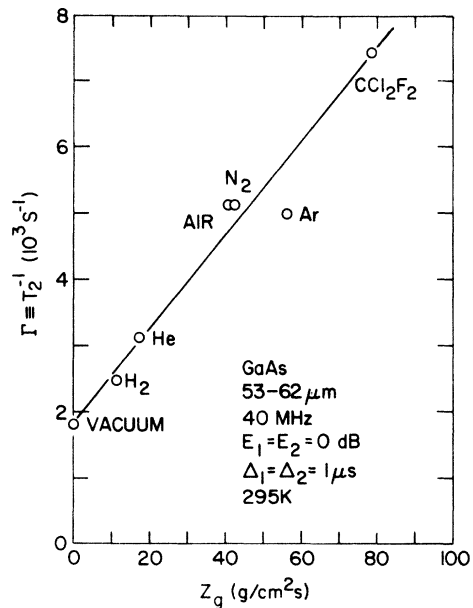


FIG. 33. Damping constant $\Gamma = T_2^{-1}$ vs acoustical impedance Z_g of the gas in which the sample is immersed at one atmosphere pressure. Pulse amplitude of 0 dB corresponds to 620-V peak across the 1-mm sample.

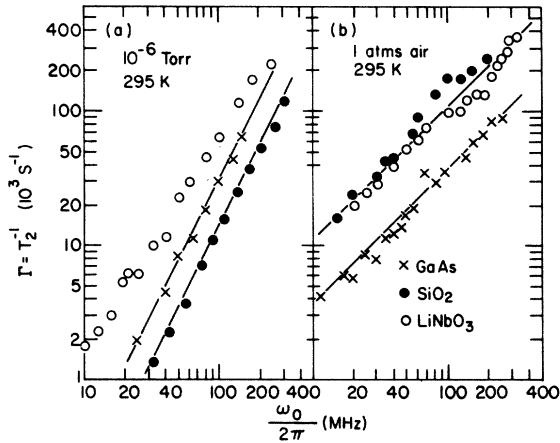


FIG. 34. Damping constant $\Gamma = T_2^{-1}$ vs frequency in LiNbO_3 (○), GaAs (×), and SiO_2 (●). (a) Sample held in vacuum of 10^{-6} Torr. (b) Sample in air at one atmosphere pressure. In (a) the solid lines have a slope of two, whereas in (b) the solid lines have a slope of one.

$10 < \omega_0/2\pi < 300$ MHz is shown in Fig. 34 for LiNbO_3 , GaAs , and SiO_2 , both in vacuum and in air at a pressure of one atmosphere. Since the losses to the gas vary linearly with frequency and the intrinsic loss can be expected to vary quadratically with frequency, T_2^{-1} can be expected to vary with frequency as

$$T_2^{-1} = (Z_g/Z_s)(\omega_0/\pi) + c\omega_0^2, \quad (35)$$

where c is a measure of the intrinsic loss mechanism. The straight lines in Fig. 34(a) correspond to a slope of two indicating that the intrinsic loss mechanism dominates as expected in a vacuum. (For LiNbO_3 , there appears to remain some contribution to the loss at low-frequency varying linearly with ω_0). In Fig. 34(b) the straight lines

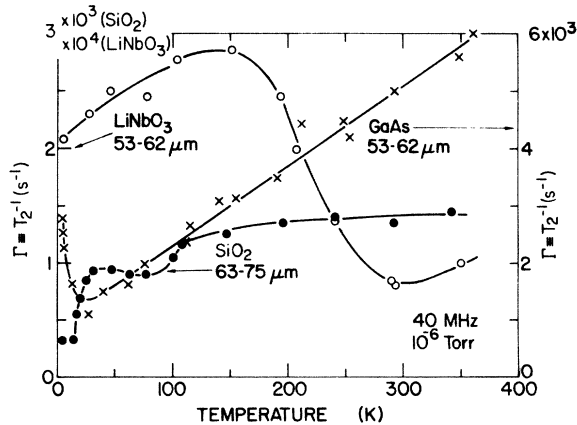


FIG. 35. Temperature dependence of the damping constant $\Gamma = T_2^{-1}$ for GaAs (×), LiNbO_3 (○), and SiO_2 (●) powder.

have a slope of one indicating that the surface losses dominate the decay in the frequency range considered when the particles are immersed in air at one atmosphere.

The temperature dependence of T_2^{-1} in GaAs , LiNbO_3 , and SiO_2 is indicated in Fig. 35. In making these measurements care was taken to ensure thermal equilibrium of the sample and to prevent condensation of gas molecules onto the powder particles. This latter problem was most easily avoided by doing the measurement in vacuum. The data are rather unremarkable except for some weak temperature dependence which may be associated with unintentional residual gas condensation or with absorption due to defects in the particles. Because of the wide variety of particle geometries and modes, the measurement of T_2^{-1} is a good way to determine mechanical losses in a powdered material only when all standard techniques are not applicable.

V. EXPERIMENTAL RESULTS: MICROWAVE FREQUENCIES

Experiments on polarization echoes in single crystals, at microwave frequencies, generally require high-input pulse powers and high- Q resonant cavities in order to obtain fields of order 100 V/cm. However, in powders the echoes are orders of magnitude stronger, undoubtedly because the particles themselves are high- Q resonators ($Q \approx 10^5$ in some of our experiments). In ZnO , at our lowest temperature, 1.25 K, echo signals 10 dB above noise could be observed in a shorted waveguide using 100-ns pulses of peak power, $P \approx 10$ mW (i.e., 50 dB < 1 kW), corresponding to $E \approx 1$ V/cm.

In all of the following, unless otherwise noted, input powers and fields will be stated in dB below 1 kW. Also, unless otherwise noted, $\Delta_1 = \Delta_2 = 100$ ns. The oscilloscope photographs of echo decays were all made with the time of E_2 fixed and τ was varied by changing the timing of E_1 . Therefore, the time scale is τ , not 2τ . Also, since the photographs only illustrate qualitative behaviors, the receiver gain was adjusted to fill the picture area as nearly as possible.

A. Low temperatures

1. Power dependence

Figure 36 illustrates the dependence of the echo decay envelope on E_2 , keeping E_1 fixed. When E_2 is greater than E_1 the decay envelope of the 2τ echo has the simple behavior predicted by small-signal theory, and the 3τ echoes are very small. When E_2 is reduced below E_1 a sharp minimum

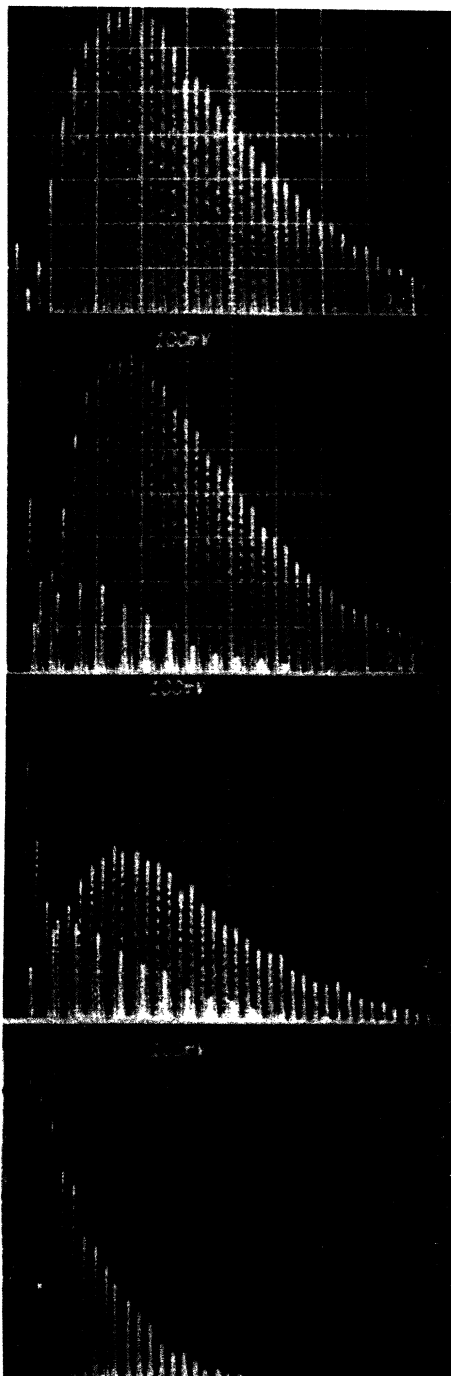


FIG. 36. Echo decay envelopes for various E_2 with $E_1 = -24$ dB. 3τ echoes are easily distinguished on the second and third pictures. Time scale is $\tau = 2\mu\text{s}/\text{cm}$ (not 2τ). Top to bottom: $E_2 = -42, -33, -26,$ and -20 dB. ZnO: 8.6 GHz, 1.25 K, $\Delta_1 = \Delta_2 = 100$ ns.

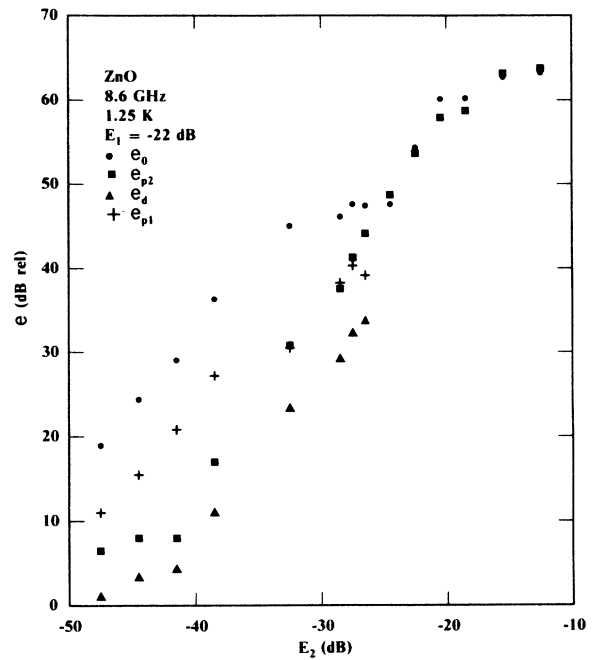


FIG. 37. Relative values of e_0, e_{p1}, e_{p2}, e_d vs E_2 for $E_1 = -22$ dB. ZnO: 8.6 GHz, 1.25 K, $\Delta_1 = \Delta_2 = 100$ ns.

followed by a broad second maximum appears in the 2τ decay, and the 3τ echoes become relatively much larger. As E_2 is reduced further the minimum, e_d , deepens, and its position τ_d moves toward smaller τ . The second maximum e_{p2} becomes relatively larger compared with the first maximum e_{p1} . Its position τ_{p2} remains stationary (note that this differs from Fig. 23) as does that of the first

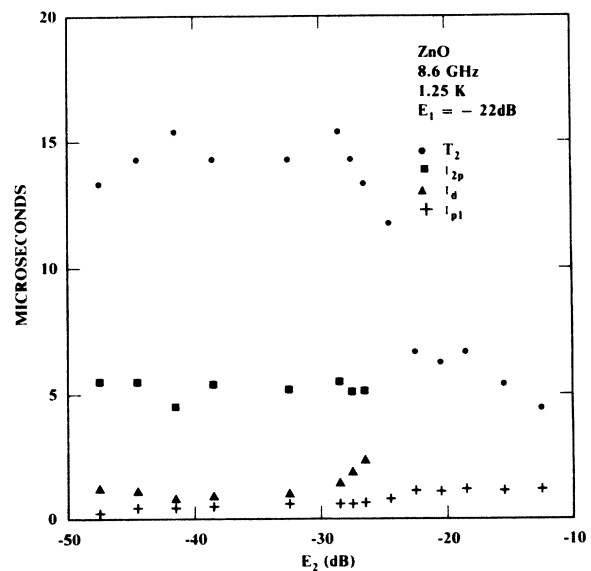


FIG. 38. $T_2, \tau_{p2}, \tau_d, \tau_{p1}$ vs E_2 for $E_1 = -22$ dB. ZnO: 8.6 GHz, 1.25 K, $\Delta_1 = \Delta_2 = 100$ ns.

peak τ_{p1} . The amplitude of the 3τ echoes again becomes relatively small at small E_2 .

Quantitative results are shown in Figs. 37 and 38. Figure 37 shows e_0 [the value of $e(2\tau)$ extrapolated to $\tau=0$; see Sec. III], e_{p1} , e_{p2} , and e_d vs E_2 , for $E_1 = -24$ dB. The principal feature is that at low E_2 all four amplitudes vary as E_2^2 , although e_{p1} and e_d start out more slowly. At large E_2 ($E_2 > E_1$), e_0 and e_{p1} level off; e_{p2} folds over, and tends toward coalescence with e_d at $E_2 = E_1$. Figure 38 shows T_2 , τ_{p2} , τ_d , and τ_{p1} vs E_2 . While, as stated above, τ_{p2} and τ_{p1} are relatively constant, with increasing E_2 , τ_d is constant at first, but then increases toward τ_{p2} before they become indistinguishable at $E_2 \simeq E_1$. The most striking feature of Fig. 38, however, is the rapid decrease in T_2 as E_2 increases through E_1 . This is probably an artifact of the measurement method, since for this power range T_2 is measured at smaller τ than it was when $E_2 < E_1$ and the second maximum was observable.

The variations of amplitudes and times at low powers are all indicative of small-signal behavior. However, the overall envelope behavior is, of course, at variance with small-signal theory, as is also the sudden decrease (Fig. 36) in the ratio $e_2(3\tau)/e_2(2\tau)$ as E_2 increases through E_1 .

2. Amplitudes

In Fig. 39 we show the qualitative behavior of the echo decay envelope for E_2 maintained at 5 dB below E_1 , varying both E_1 and E_2 together. A strong similarity to Fig. 36 is obvious. However, in the present case the envelope has a single maximum at low powers; as the powers are increased the minimum moves out from $\tau=0$ and continues toward larger τ_d , the original maximum also moves toward larger τ , while a new first maximum moves out from $\tau=0$ and its amplitude increases relative to that of the second maximum.

Referring to Fig. 40, it is seen that at low powers e_0 and e_{p2} increase approximately linearly with E_1 with E_2 maintained at 5 dB below E_1 . e_{p2} and e_d fold over and eventually disappear in the noise as E_2 is further increased, while e_{p1} increases as E_2^{1-3} in this region. The dependence of T_2 , τ_{p2} , and τ_d are shown in Fig. 41. They all increase monotonically with increasing E_1 . τ_{p1} remains constant once this peak becomes distinguishable. After e_d and e_{p2} vanish there is an apparent decrease in T_2 (not shown), but this is really the fast decay of e_{p1} .

Unlike the previous data ($E_1 = \text{const}$), the low-power behavior for this case does not indicate small-signal behavior, even though both fields (E_1 and E_2) are smaller at the low end than pre-

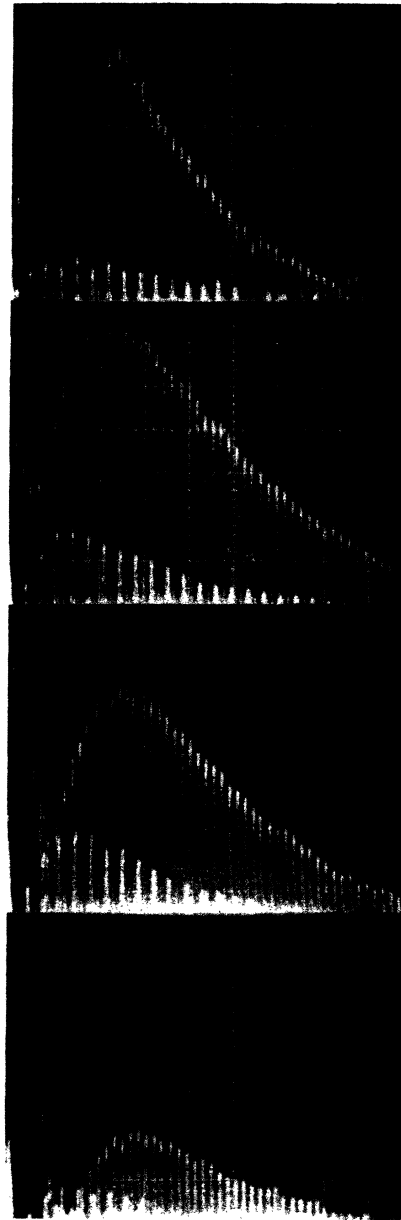


FIG. 39. Decay envelopes for various E_1 with E_2 maintained 5 dB below E_1 . 3τ echoes are also observable. Time scale: $\tau = 2 \mu\text{s}/\text{cm}$. Top to bottom: $E_1 = -40, -25, -22, \text{ and } -19$ dB. ZnO: 8.6 GHz, 1.25 K, $\Delta_1 = \Delta_2 = 100$ ns.

viously. Small-signal theory predicts $e_0 \propto E_1 E_2^2 \propto E_1^3$ rather than $e_0 \propto E_1$ as observed. Also small-signal theory cannot predict the monotonic increase in T_2 or τ_{p2} .

3. Phase measurements

Relative phase measurements were made on the echo signals by the method outlined in Sec. III.

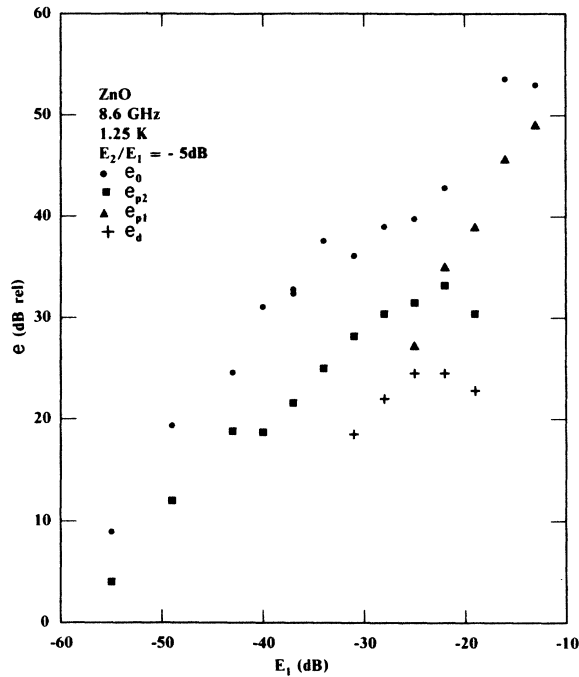


FIG. 40. e_0 , e_{p2} , e_{p1} , and e_d vs E_1 with E_2 maintained at 5 dB below E_1 . ZnO: 8.6 GHz, 1.25 K, $\Delta_1 = \Delta_2 = 100$ ns.

The principal results of these measurements are: (i) whenever a minimum occurs in the decay envelope the phases on either side of the minimum differ by approximately π as shown in Fig. 42. This result holds regardless of the relative depth of the minimum. In the temperature range 3–5 K at X band, minima were observed with $E_2 > E_1$ as well as $E_2 < E_1$ ($\Delta_1 = \Delta_2$), but the former only with E_2 and E_1 both so small that the signal-to-noise ratio was very poor. However, in this case also phase reversal occurred. (ii) At the minimum the

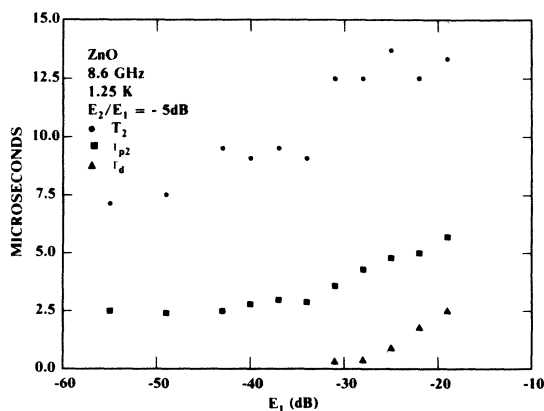


FIG. 41. T_2 , τ_{p2} , and τ_d vs E_1 and E_2 maintained at 5 dB below E_1 . ZnO: 8.6 GHz, 1.25 K, $\Delta_1 = \Delta_2 = 100$ ns.

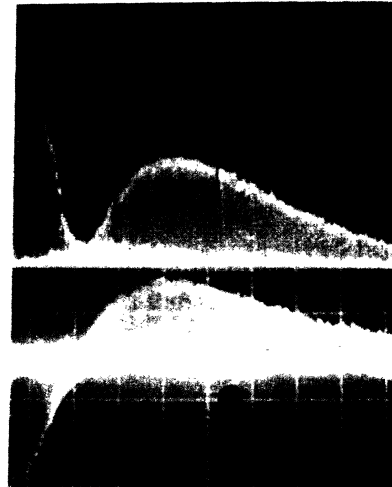


FIG. 42. e_2 vs τ with E_1 5 dB greater than E_2 . ZnO: 1.25 K, 9.0 GHz, $\Delta_1 = \Delta_2 = 50$ ns. Top: amplitude detection. Bottom: phase-sensitive detection adjusted for zero phase on the second-envelope maximum.

echo phase is in quadrature with the phases at the maxima as may be seen in Fig. 43. (iii) In the absence of a minimum the phase varied very little throughout the decay envelope. (iv) The phase variation across an individual echo signal is only slight (at least when $\Delta_1 = \Delta_2$) even in the neighborhood of the minimum where the echo shape is changing rapidly (see Fig. 43 and below). (v) For the experimental conditions used, the 3τ echo is in quadrature with the 2τ echo, as shown in Fig. 43.

4. Echo shapes

Unlike the VHF data the X-band results in ZnO show only slight evidence of multiple peaks and never a central minimum as long as $\Delta_1 = \Delta_2$ (see Fig. 43). This result was established over the range $\Delta_1 = \Delta_2 = 20$ –300 ns, although complex decay behavior was observed over this whole range. Complex echo shapes were, however, observed with $\Delta_1 > \Delta_2$. Some examples are shown in Fig. 44 for $\Delta_1 = 300$ ns and various $\Delta_2 \leq \Delta_1$. In general, however, the decay envelopes were unaffected in any way which could not be accounted for, at least qualitatively, on the basis of the areas $E_1\Delta_1$ and $E_2\Delta_2$.

Referring again to Fig. 43, it is seen that the echo shape changes from roughly triangular with shoulders to a more flat-topped configuration as the minimum is traversed. It is also interesting that the shape changes observed with in-phase detection are roughly opposite to those observed with quadrature detection, e.g., in the former case shoulders appear for $\tau < \tau_d$ and flat-topped shapes

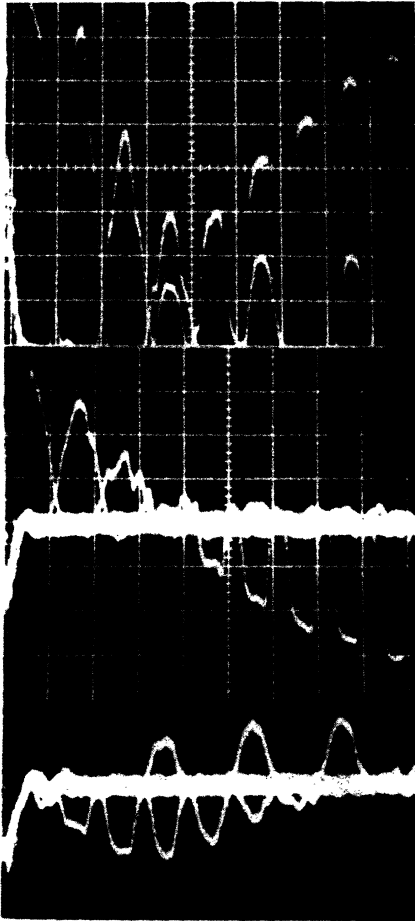


FIG. 43. e_2 vs τ for E_1 6 dB greater than E_2 in the neighborhood of the envelope minimum ZnO: 1.25 K, 9.06 GHz, $\Delta_1 = \Delta_2 = 300$ ns. Top: amplitude detection. Middle: phase-sensitive detection adjusted for zero phase on the second-envelope maximum. Bottom: phase-sensitive detection with reference 90° out of phase with that above. 3τ echoes are distinguishable by their larger interecho spacing.

for $\tau > \tau_d$, while in quadrature detection the inverse occurs.

B. Temperature dependences

Both e_0 and T_2 decrease with increasing temperature. Figure 45 is a log-log plot of e_0 and T_2^{-1} vs T for 8.66 GHz from $T = 1.25$ to 21 K; 17-GHz data in T_2^{-1} are also shown from $T = 1.25$ to 4.2 K. The data were taken with E_2 1 dB $< E_1$ in order to avoid the complex decay envelopes associated with $E_2 < E_1$. The latter are extremely temperature dependent as seen in Fig. 46. Also, relatively high-input fields were utilized in order to minimize the power dependence of T_2 and still have a measurable echo at the higher temperatures.

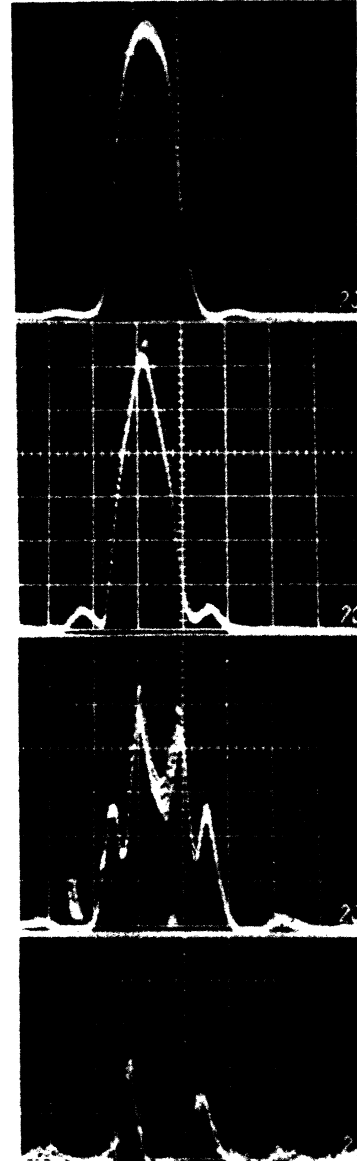


FIG. 44. Representative echo shapes for $\Delta_1 = 300$ ns and various Δ_2 . τ slightly greater than τ_d ($\Delta_2 = 300$ ns). E_1 3 dB greater than E_2 . ZnO: 8.8 GHz, 1.25 K. Top to bottom: $\Delta_2 = 300, 200, 100,$ and 50 ns.

Referring to Figs. 46 and 47, for which $E_1 \Delta_1$ is 8 dB greater than $E_2 \Delta_2$, the decay envelope exhibits the usual (under this condition) minimum with two maxima. However, e_d is barely less than e_{p2} at 1.25 °K. All four amplitudes e_0 , e_{p1} , e_{p2} , and e_d increase as T is increased from 1.25 K to between 2 and 3 K and then decrease upon further increasing T . The ratio e_{p1}/e_{p2} increases, as does e_{p2}/e_d , causing the minimum to be more pronounced. The general behavior is somewhat similar to the power dependences discussed earlier.

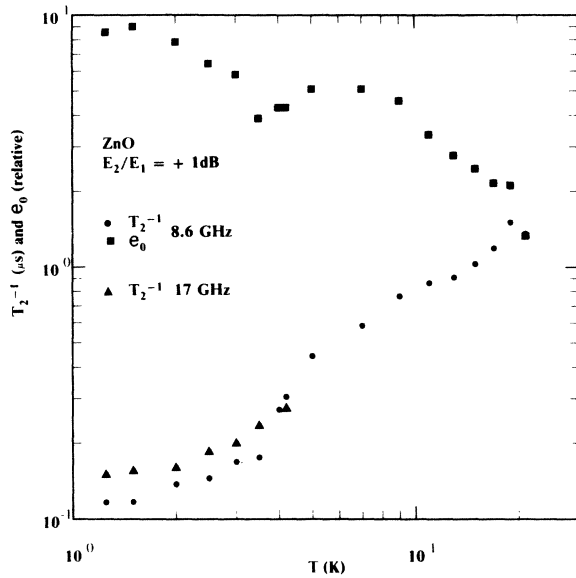


FIG. 45. e_0 and T_2^{-1} vs T , 8.6 GHz, and T_2^{-1} vs T , 17 GHz, ZnO.

However, in contrast to the latter, τ_d and τ_{p2} are nearly independent of T , while T_2 decreases monotonically as may be seen in Fig. 48.

Figures 49 and 50 show the dependences of the amplitudes and times on temperature when $\Delta_1 = \Delta_2$ and E_2 is 1 dB greater than E_1 . Under this condition the envelope decay exhibits the simple single-peaked behavior. e_0 and e_p decrease rapidly with temperature above 2.5 K; T_2 and τ_p decrease monotonically over the whole range of T .

Similar behaviors were observed at X band. However, at Ku band we could never find a set of values for E_1 and E_2 which would produce a deep minimum with distinct maxima at temperatures under 2.5 K. In general, to obtain qualitatively similar echo-decay envelopes the power had to be lower and the temperature higher at Ku band.

C. Results at 9 K

The parameter L of Eq. (26), which is a measure of the small-signal to large-signal transition, is inversely proportional to Γ if $\Gamma\tau \gg 1$. Thus, we might expect to observe the small-signal regime at higher temperatures in measurements of e_0 (which, as explained in Sec. IV is extrapolated from data at $\Gamma\tau > 1$). Furthermore, above $T \approx 6$ K in ZnO at X - and Ku -band frequencies, we have never observed complex decay behavior regardless of the relative values of E_1 and E_2 . Two representative decay envelopes are shown in Fig. 51.

The dependences of e_0 on power at 8.6 GHz for both E_2 5 dB less than E_1 , and E_2 1 dB greater than E_1 (E_1 and E_2 varied together) are presented in

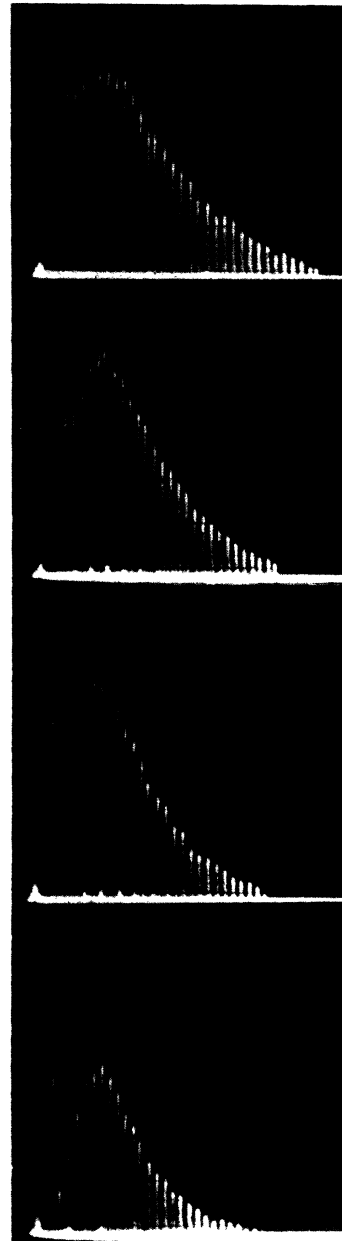


FIG. 46. Decay envelopes with E_1 8 dB greater than E_2 and $\Delta_1 = \Delta_2 = 100$ ns, for various temperatures. Top to bottom: $T = 1.25, 2.5, 3,$ and 3.5 K. ZnO: 17 GHz, $2 \mu\text{s/cm}$.

Fig. 52. In both cases $e_0 \propto E^3$ at low powers, as expected for small signals. However, it should be noted that e_0 (E_2 5 dB $> E_1$) is larger than e_0 (E_2 1 dB $< E_1$) for equal values of E_1 , whereas an $E_1 E_2^2$ dependence would predict the former to be 12 dB smaller than the latter. This suggests that the strength of the nonlinearity is itself dependent in a complicated way on E_1 and E_2 .

Figure 53 shows that T_2 is power dependent (see

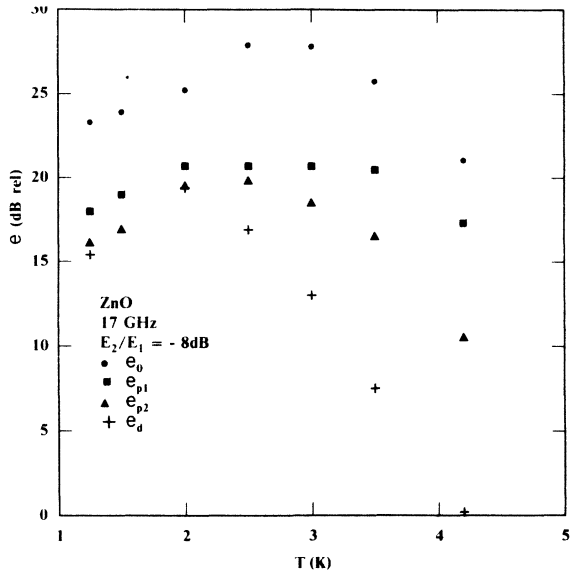


FIG. 47. e_0, e_p, e_{p2}, e_d vs T . $E_1 = -6$ dB, $E_2 = -14$ dB, $\Delta_1 = \Delta_2 = 100$ ns. ZnO: 17 GHz.

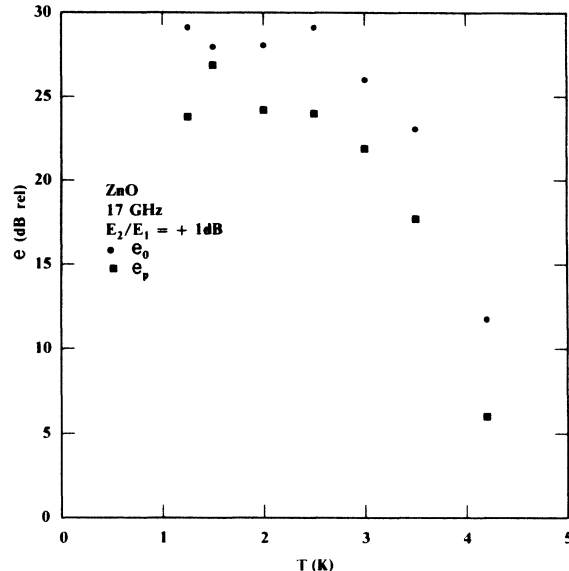


FIG. 49. e_0, e_p vs T . $E_2 = -14$ dB, $\Delta_1 = \Delta_2 = 100$ ns. ZnO: 17 GHz.

Fig. 51 also), and the variation is greatest at low powers under either condition of the ratio E_1/E_2 . This is, of course, at variance with small-signal theory. In addition, comparison with the 1.25-K data shows that although T_2 is smaller at 9 K, 1.25-K measurements which did not exhibit small-signal behavior were made at power levels as much as 30 dB smaller than those at 9 K. This is sufficiently smaller that $L(9\text{ K}) > L(1.2\text{ K})$.

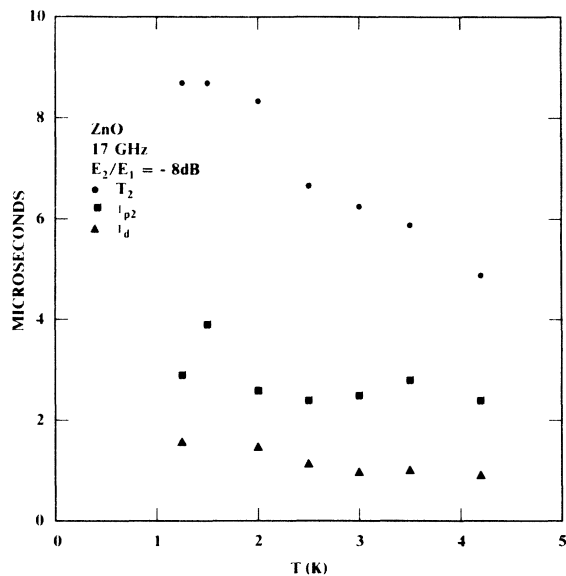


FIG. 48. T_2, τ_{p2}, τ_d vs T . $E_1 = -6$ dB, $E_2 = -14$ dB, $\Delta_1 = \Delta_2 = 100$ ns. ZnO: 17 GHz.

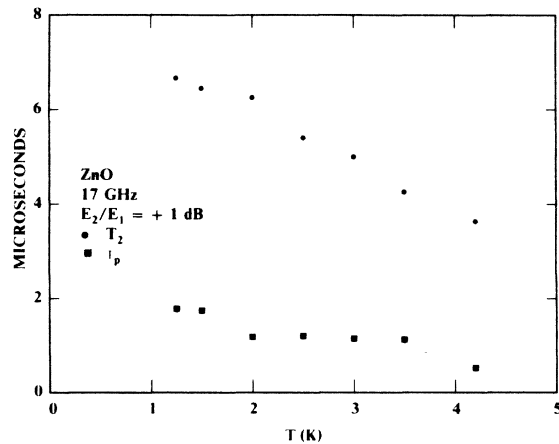


FIG. 50. T_2, τ_p vs T . $E_1 = -15$ dB, $E_2 = -14$ dB, $E_2 = -14$ dB, $\Delta_1 = \Delta_2 = 100$ ns. ZnO: 17 GHz.

D. Results on diluted samples

All of the data presented above were made on samples of the type described in Sec. III B, containing only ZnO powder. In order to test the possibility that some of the complex results might be due to interparticle interactions involving all (or a large number of) the particles, some samples were diluted with Al_2O_3 powder (average particle size less than $1\ \mu$). It was first ascertained that echoes were not observed in pure Al_2O_3 samples, as expected since Al_2O_3 is not piezoelectric. Dilution ratios ZnO/ Al_2O_3 equal to 3, 1, $\frac{1}{3}$, $\frac{1}{10}$, $\frac{1}{30}$ were all tried. No effects of dilution, other than the expected reduction in signal amplitude, were found.

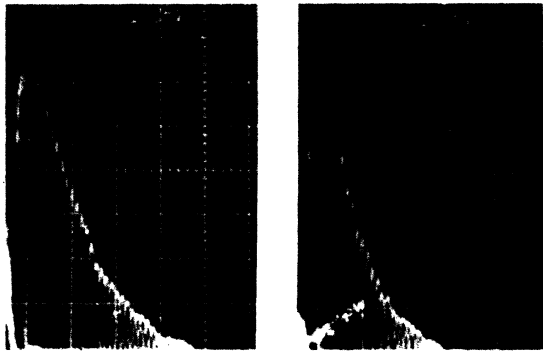


FIG. 51. Echo-decay envelopes at 9 K and E_1 5 dB greater than E_2 . Time scale: 500 ns/cm. Left: $E_1 = -8$ dB. Right: $E_1 = -20$ dB. ZnO: 8.6 GHz, $\Delta_1 = \Delta_2 = 100$ ns.

E. Discussion of results at microwave frequencies

For ZnO, the data of Fig. 45 show that at the lowest temperatures T_2^{-1} , which is presumed to be proportional to the ultrasonic mode damping, becomes temperature independent. This suggests (as is often the case in bulk microwave ultrasonic experiments) the presence of a temperature-independent component of the damping, such as might arise from geometrical effects or surface scattering. In Fig. 54 we have subtracted off the 1.25-K damping, and presented the 8.6-GHz results on an Arrhenius plot. The reduced data indicate an activated damping mechanism with an activation energy $\epsilon/k_B \approx 11$ K. This kind of damping would be expected from a relaxation mechanism, $T_2^{-1} \propto 1/\tau_R$ in the region $\omega\tau_R \gg 1$, with $\tau_R^{-1} \propto \exp(-\epsilon/k_B T)$. This damping mechanism also agrees with the near independence of T_2 on frequency (Fig. 45). It would

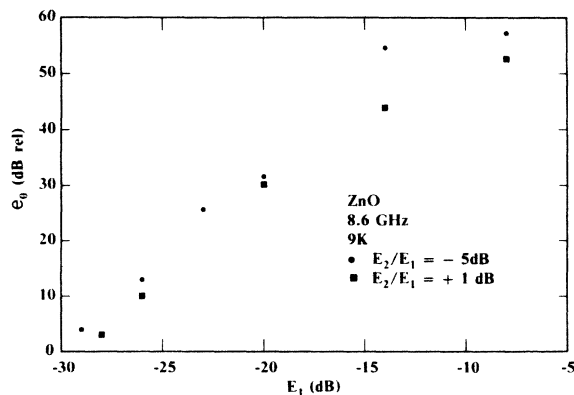


FIG. 52. e_0 vs E_1 for $E_2/E_1 = -5$ dB and $E_2/E_1 = +1$ dB. ZnO: 8.6 GHz, 9 K, $\Delta_1 = \Delta_2 = 100$ ns.

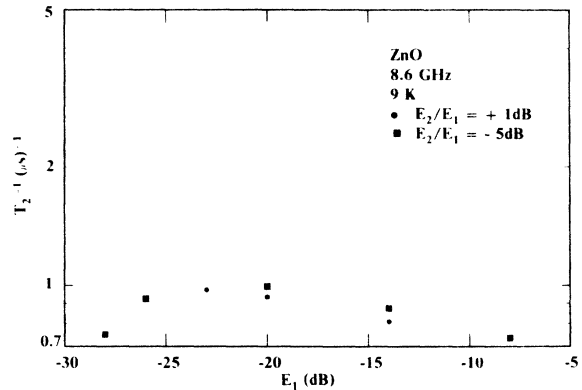


FIG. 53. T_2^{-1} vs E_1 for $E_2/E_1 = -5$ dB and $E_2/E_1 = +1$ dB. ZnO: 8.6 GHz, 9 K, $\Delta_1 = \Delta_2 = 100$ ns.

also explain, for the same reason, the decrease of e_0 with increasing T . At this time, however, it is not known to what extent the power dependence of T_2 would influence the temperature dependence.

The fact that T_2 is power dependent can indicate either power-dependent damping, or be merely a reflection of a complicated dependence of the non-linearity upon the particle oscillation amplitudes, e.g., the more rapid increase with applied field at large τ than at small τ (thereby increasing the

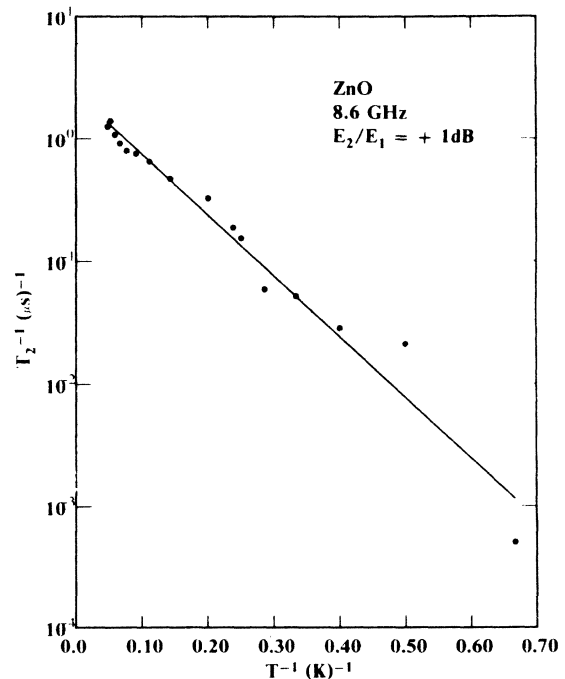


FIG. 54. T_2^{-1} vs T^{-1} after subtracting off the 1.25 K value. Solid line is $T_2^{-1} \propto e^{11/T}$.

apparent T_2) could be due to the fact that the oscillation amplitude is smaller at large τ and the field dependence is greater for small fields (and therefore for small oscillation amplitudes). At any rate, it is worth noting that power-dependent damping is a nonlinear process which can itself give rise to echoes (see Sec. III). Computations⁶⁷ for a model saturable absorber of the relaxation type, using δ -function pulses, are in agreement with many of the results, including the observed complex behavior of the decay envelopes, as well as the temperature and power dependences of T_2 , but not the lack of agreement with very-small-signal theory.

VI. CONCLUSIONS

In Sec. III the differences between anharmonic-oscillator models and parametric field-mode interaction models were pointed out. All of our experimental data clearly show that the echoes are caused by an anharmonic-oscillator mechanism. However, many examples of anharmonic oscillators can be given which are indistinguishable in the small-signal limit. These are in partial agreement with experiment in that limit, but only at the lowest applied pulse amplitudes consistent with adequate signal to noise. A limited number of calculations were carried out in the large-signal limit using δ -function pulses (see Ref. 61). Although these predict such effects as the natural occurrence of multiple two-pulse echoes and their decay properties, as well as complex echo shapes, and complicated decay behavior, they do not agree with many of the observed properties of the echoes at high or even moderate powers. It is not yet clear whether the observed discrepancies arise because of the approximations made in evaluation of the model (i.e., δ -function pulses, small-signal limit, neglect of nonlinearity under the pulse, neglect of the distribution of $\Gamma = T_2^{-1}$, neglect of the distribution of particle orientations, . . .) or because of basic inadequacies in the model itself. As discussed in Sec. V E, the temperature and power dependences observed in ZnO powder at X band bear some similarity to those expected on the basis of an anharmonic oscillator of the saturable relaxation absorber type.

The most significant conclusions to be drawn from this study can be summarized as follows: (i) the irregular ringing signal radiated by a powder sample after a single pulse excitation is the consequence of incomplete phase cancellation of the linear mechanical oscillations of the piezoelectric particles. This ringing is not related to the coherent free-induction decay radiated by a spin system after a single pulse excitation. (ii)

The decay behavior of the echoes caused by a parametric field-mode interaction is distinctly different from that for echoes generated by an anharmonic-oscillator system. (iii) The experimental data presented here on dynamic echoes in SiO₂, GaAs, LiNbO₃, and ZnO are clearly caused by an anharmonic-oscillator mechanism and not by a parametric field-mode interaction. (iv) A specific anharmonic-oscillator model was described in detail in the small-signal limit with pulses of finite width and in the large-signal limit for δ -function pulses. Agreement between the small-signal theory and experiment is achieved only in GaAs powder in the VHF band at the lowest powers attainable consistent with adequate signal to noise. Discrepancies found between experiment and small-signal theory in other powders indicates that the small-signal limit was not reached in those materials or that the particular type of anharmonic-oscillator model chosen was incorrect. In the large-signal limit no anharmonic-oscillator model has yet been fully analyzed. Consequently, it is not yet known to what extent the rather complex large-signal behavior can be understood on the basis of the particular model described in Sec. II C or any other. (See, however, Ref. 61.) (v) Results at X band on samples of ZnO diluted with Al₂O₃ powder showed that interparticle interactions do not play a role in echo behavior. (vi) Single pulse "edge echoes" are detected when using high amplitude, wide pulses. (vii) The decay time T_2 is found to be a sensitive function of particle surface preparation. On etching GaAs powder, T_2 was found to increase two orders of magnitude. (viii) Both the decay time T_2 and the echo amplitude were found to be relatively independent of temperature for $4.2 < T < 400$ K in the VHF band. However, in ZnO at microwave frequencies, T_2 shows a marked dependence upon temperature which agrees with the supposition of a relaxation type damping with activation energy/ $k_B \approx 11$ K. (ix) When contained in vacuum the decay constant $\Gamma \equiv T_2^{-1}$ was found to increase quadratically with frequency in the VHF band indicating a volume loss mechanism. (x) When immersed in air at one atmosphere $\Gamma \propto \omega$ in the VHF band indicating a surface transmission loss mechanism. Measurements made in gases of different acoustical impedances in the VHF band are in reasonable quantitative agreement with a calculation of the loss associated with the transmission of the mechanical energy to the gas through the particle surface.

ACKNOWLEDGMENTS

We are indebted to D. R. Vigliotti for his expert technical support of this work and to C. F. Aliotta

for the electron micrographs of ZnO powders. One of the authors (KF) would like to acknowledge the partial support of the Norwegian Research Council for Science and Humanities. One of the authors (NSS) wishes to thank Dr. W. B. Mims for having pointed out the efficacy of low-noise TWT receivers in echo spectrometers.

APPENDIX A

The simplest phenomenological parametric field-mode interaction of interest⁴⁸ is of the form

$$U_{\text{FM}} = \frac{1}{2} \gamma_6 E_{\text{in}}^2 S^2, \quad (\text{A1})$$

where the nonlinear constant γ_6 is a component of a sixth-rank tensor. The wave equation for the displacement in the presence of the field E_{in} is

$$\ddot{u} + 2\Gamma\dot{u} - \frac{c_2}{\rho} u_{xx} - \left(\frac{\gamma_6}{\rho}\right) E_{\text{in}}^2 u_{xx} = -\frac{1}{\rho} \frac{\partial}{\partial x} (E_{\text{in}}). \quad (\text{A2})$$

Assuming a solution of the form given by Eq. (4a) and the applied field given by Eq. (10), the following first-order equation for the amplitude $a(t)$ is valid in the slowly varying envelope approximation.

$$\dot{a} + [\Gamma - i(\omega_0 - \Omega)]a - i\gamma_{\text{FM}} a^* = i\beta E_{\text{in}}(\pm b, t) \exp[i\omega_0(t - t_0)], \quad (\text{A3})$$

where

$$\Omega = \Omega_0 [1 + (\gamma_6/c_2) E_{\text{in}}^2(\pm b, t)], \quad (\text{A4})$$

$$\gamma_{\text{FM}} = (\gamma_6/2c_2) \Omega_0 E_{\text{in}}^2(\pm b, t), \quad (\text{A5})$$

and Ω_0 is given by Eq. (7b). The right-hand side of Eq. (A3) corresponds to linear surface piezoelectric excitation of the particle. For parametric field-mode interactions the linear excitations caused by the second pulse are of no interest and can be neglected. The solution to Eq. (A3) with the right-hand side set equal to zero is

$$a(t) = \{a(t_0) \cosh(\gamma_{\text{FM}}^2 - \omega^2)^{1/2} (t - t_0) + i\Delta [a(t_0)\omega + a^*(t_0)\gamma_{\text{FM}}]\} [\sinh(\gamma_{\text{FM}}^2 - \omega^2)^{1/2} (t - t_0) / (\gamma_{\text{FM}}^2 - \omega^2)^{1/2} \Delta] \exp[-i(\omega_0 - \Omega)(t - t_0)]. \quad (\text{A6})$$

with ω given by Eq. (11e).

The initial condition $a(t_0)$ for Eq. (A6) is determined by the linear excitation $a_{\Delta 1}$ caused by the first pulse. Setting $t_0 = \tau$ we have

$$a(\tau) = a_{\Delta 1} e^{-(\Gamma + i\Omega_0)\tau}, \quad (\text{A7})$$

$$a(t) = \{a_{\Delta 1} \cosh(\gamma_{\text{FM}}^2 - \omega^2)^{1/2} \Delta_2 + i\Delta_2(\omega a_{\Delta 1} + \gamma_{\text{FM}} a_{\Delta 1}^* e^{2i\Omega_0\tau}) \times [\sinh(\gamma_{\text{FM}}^2 - \omega^2)^{1/2} \Delta_2 / (\gamma_{\text{FM}}^2 - \omega^2)^{1/2} \Delta_2]\} \exp[-\Gamma t - i\Omega_0(t - \Delta_2) + i\omega_0(t - \tau - 2\Delta_2)], \quad (\text{A8})$$

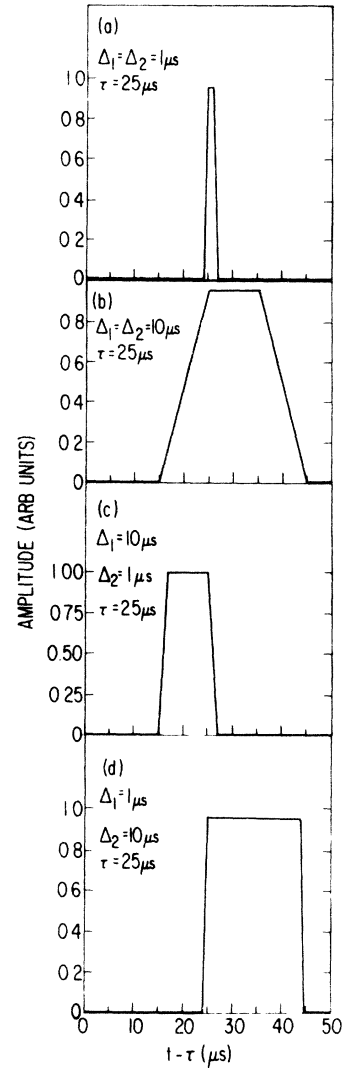


FIG. 55. Two-pulse echo shapes and positions computed for the parametric field-mode interaction from Eq. (A10) in a small-signal limit. Amplitude plotted vs $t - \tau$ with $\tau = 25$, μs , $T_2 = 1000$ μs and (a) $\Delta_1 = \Delta_2 = 1$ μs ; (b) $\Delta_1 = \Delta_2 = 10$ μs ; (c) $\Delta_1 = 10$ μs , $\Delta_2 = 1$ μs ; (d) $\Delta_1 = 1$ μs , $\Delta_2 = 10$ μs .

where $a_{\Delta 1}$ is given by Eq. (11b). Using Eq. (A6) evaluated at $t = \tau + \Delta_2$ (i.e., at the end of the second pulse) as the initial condition for the solution to the free linear oscillator [Eq. (11a)], the amplitude for $t > \tau + \Delta_2$ is given by

where the amplitude a_{Δ_2} , linearly excited by the second pulse, has been neglected since it cannot contribute to the two-pulse echo. Inserting Eq. (A8) into Eq. (16) we obtain the following expression for the coherent response of the powder:

$$V(t) = -\frac{1}{4} \frac{K^2}{(1+K^2)^3} \gamma_6 \omega_0 \frac{A m^2(b)}{b^3} \frac{\epsilon_0^3}{\rho \epsilon^2} E_1 E_2^2 \Delta_1 \Delta_2 \exp[-2\Gamma\tau - i\omega_0(t-2\tau)] \\ \times \int_{-\infty}^{\infty} d\omega G_R(\omega) G_\omega(\omega) \int_0^\pi d\theta \sin\theta \cos^4\theta G_1^*(\xi) [\sinh(\gamma_{FM}^2 - \omega^2)^{1/2} \Delta_2 / (\gamma_{FM}^2 - \omega^2)^{1/2} \Delta_2] e^{i\omega(t-2\tau-\Delta_2)}, \quad (\text{A9})$$

where $G_1(\xi)$ is given by Eq. (11c), E_{in} has been replaced by Eq. (8), and γ_{FM} is given by Eq. (A5).

$V(t)$ is nonzero only for $t \approx 2\tau$.

From Eq. (A9) the following conclusions concerning this parametric field-mode interaction can be reached: (i) Only an echo at $t=2\tau$ is obtained, echoes at $t=m\tau$, $m=3\tau, 4\tau, \dots$, cannot arise from an interaction of the form given by Eq. (A1). (ii) The 2τ echo amplitude decays monotonically with the pulse separation τ as $\exp(-2\Gamma\tau)$. (iii) In the small-signal limit the integrals are easily evaluated to give the echo shapes which are shown in Fig. 55. Note the difference between these shapes and those in Fig. 4 calculated for the anharmonic oscillator. (iv) In the high-amplitude limit $[\gamma_{FM} \gg (T_2^*)^{-1}]$, where $(T_2^*)^{-1}$ is the half-width of the

distribution of natural frequencies $G_\omega(\omega)$] the echo amplitude increases with the second-pulse amplitude as $\sinh \gamma_{FM} \Delta_2$. Thus for $\gamma_{FM} \Delta_2 > 1$ the echo increases exponentially with E_2^2 [see Eq. (A5)].

(v) An analysis for a three-pulse sequence reveals that a stimulated three-pulse echo at $t=T+\tau$ cannot arise from an interaction of the form of Eq. (A1). (vi) An "image"¹ three-pulse echo at $t=2T-2\tau$ does follow from Eq. (A1).

The existence of both $m\tau$ two-pulse echoes ($m > 2$) and stimulated three-pulse echoes is an acknowledged property of dynamic echoes in powders. Therefore, we conclude that a parametric field-mode interaction of the type given by Eq. (A1) cannot even qualitatively explain the existence of dynamic polarization echoes in powders.

*Present address: Dept. of Physics, The Norwegian Institute of Technology, 7034 Trondheim, Norway.

†Present address: Electrotechnical Laboratory, Tanashi, Tokyo 188, Japan.

¹E. L. Hahn, *Phys. Rev.* **80**, 580 (1950).

²Richard J. Blume, *Phys. Rev.* **109**, 1867 (1958).

³J. P. Gordon and K. D. Bowers, *Phys. Rev. Lett.* **1**, 368 (1958).

⁴N. A. Kurnit, I. D. Abella, and S. R. Hartmann, *Phys. Rev. Lett.* **13**, 567 (1964); *Phys. Rev.* **141**, 391 (1966).

⁵D. E. Kaplan, *Phys. Rev. Lett.* **14**, 254 (1965).

⁶R. M. Hill and D. E. Kaplan, *Phys. Rev. Lett.* **14**, 1062 (1965).

⁷R. M. Hill, D. E. Kaplan, G. F. Herrmann, and S. K. Ichiki, *Phys. Rev. Lett.* **18**, 105 (1967).

⁸N. S. Shiren and T. G. Kazyaka, *Phys. Rev. Lett.* **28**, 1304 (1972).

⁹S. N. Popov and N. N. Krainik, *Fiz. Tverd. Tela* **12**, 3022 (1970) [*Sov. Phys.—Solid State* **12**, 2440 (1971)].

¹⁰R. B. Thompson and C. F. Quate, *J. Appl. Phys.* **42**, 907 (1971).

¹¹N. S. Shiren and R. L. Melcher, *1974 Ultrasonics Symposium Proceedings*, IEEE Cat. No. 74CHO 896-1SU, p. 558.

¹²R. L. Melcher and N. S. Shiren, *Phys. Rev. Lett.* **34**, 731 (1975); N. S. Shiren and R. L. Melcher, *J. Electron. Mater.* **4**, 1143 (1975), and references contained therein.

¹³B. Golding and J. E. Graebner, *Phys. Rev. Lett.* **37**, 852 (1976).

¹⁴M. Rubinstein and G. H. Strauss, *Phys. Lett.* **14**,

277 (1965).

¹⁵M. Rubinstein and G. H. Strauss, *J. Appl. Phys.* **39**, 81 (1968).

¹⁶F. Borsa and G. Bonera, *Boll. Soc. Ital. Fiz.* **50**, 55 (1966).

¹⁷H. Alloul and C. Froidevaux, *C. R. Acad. Sci. B* **265**, 881 (1967).

¹⁸H. Alloul and C. Froidevaux, *Phys. Rev. Lett.* **20**, 1235 (1968).

¹⁹Z. A. Pacult, P. C. Riedi, and D. P. Tunstall, *J. Phys. F* **3**, 1843 (1973).

²⁰S. Kupca and C. W. Searle, *Can. J. Phys.* **53**, 2622 (1975), and references quoted therein.

²¹I. B. Goldberg, E. Ehrenfreund, and M. Weger, *Phys. Rev. Lett.* **20**, 539 (1968).

²²E. Ehrenfreund, I. B. Goldberg, and M. Weger, *J. Appl. Phys.* **39**, 5941 (1968).

²³A. R. Kessel[†], I. A. Safin, and A. M. Gol'dman, *Fiz. Tverd. Tela* **12**, 3070 (1970) [*Sov. Phys.—Solid State* **12**, 2488 (1971)].

²⁴S. N. Popov and N. N. Krainik, *Fiz. Tverd. Tela* **14**, 2779 (1972) [*Sov. Phys.—Solid State* **14**, 2408 (1973)].

²⁵Ch. Frénois, J. Joffrin, and A. Levelut, *J. Phys. Lett. (Paris)* **35**, L221 (1974).

²⁶N. N. Krainik, V. V. Lemanov, S. N. Popov, and G. A. Smolenskii, *Fiz. Tverd. Tela* **17**, 2462 (1975) [*Sov. Phys.—Solid State* **17**, 1635 (1976)].

²⁷S. N. Popov, N. N. Krainik, and G. A. Smolenskii, *Zh. Eksp. Teor. Fiz. Pis'ma Red.* **21**, 543 (1975) [*JETP Lett.* **21**, 253 (1975)].

²⁸V. M. Berezov, Ya. Ya. Asadullin, V. D. Korepanov,

- and V. S. Romanov, *Zh. Eksp. Teor. Fiz.* **69**, 1674 (1975) [*Sov. Phys.-JETP* **42**, 851 (1975)].
- ²⁹Ya. Ya. Asadullin, V. M. Berezov, V. D. Korepanov, and V. S. Romanov, *Pis'ma Zh. Eksp. Teor. Fiz.* **22**, 285 (1975) [*JETP Lett.* **22**, 132 (1975)].
- ³⁰P. I. Kaundersma, S. Huizenga, J. Kommandeur, and G. A. Sawatzky, *Phys. Rev. B* **13**, 496 (1976).
- ³¹B. D. Laikhtman, *Fiz. Tverd. Tela* **17**, 3278 (1975) [*Sov. Phys.-Solid State* **17**, 2154 (1976)].
- ³²V. M. Berezov, Ya. Ya. Asadullin, V. D. Korepanov, and V. S. Romanov, *Fiz. Tverd. Tela* **18**, 180 (1976) [*Sov. Phys.-Solid State* **18**, 103 (1976)].
- ³³S. A. Al'tschuler, F. L. Aukhadeev, V. A. Grevtsev, and M. A. Teplov, *Pis'ma Zh. Eksp. Teor. Fiz.* **22**, 159 (1975) [*JETP Lett.* **22**, 73 (1975)].
- ³⁴A. R. Kessel', S. A. Zel'dovich, and I. L. Gurevich, *Fiz. Tverd. Tela* **18**, 826 (1976) [*Sov. Phys.-Solid State* **18**, 473 (1976)].
- ³⁵S. Kupca and C. W. Searle, *J. Appl. Phys.* **47**, 374 (1976).
- ³⁶G. A. Smolenskii, N. N. Krainik, S. N. Popov, and B. D. Laikhtman, *Ferroelectrics* **14**, 571 (1976).
- ³⁷R. L. Melcher and N. S. Shiren, *1975 Ultrasonics Symposium Proceedings*, IEEE Cat. No. 75 CHO 994-4SU, p. 672.
- ³⁸N. N. Krainik, S. N. Popov, and G. A. Smolenskii, *Akust. Zh.* **22**, 146 (1976) [*Sov. Phys.-Acoust.* **22**, 83 (1976)].
- ³⁹J. Joffrin, A. Levelut, and D. Salin, *J. Phys. (Paris)* **37**, 271 (1976).
- ⁴⁰Ch. Frénois, J. Joffrin, and A. Levelut, *J. Phys. (Paris)* **37**, 275 (1976).
- ⁴¹B. D. Laikhtman, *Fiz. Tverd. Tela* **18**, 612 (1976) [*Sov. Phys.-Solid State* **18**, 357 (1976)].
- ⁴²G. A. Sawatzky and S. Huizenga, *Appl. Phys. Lett.* **28**, 476 (1976).
- ⁴³R. L. Melcher and N. S. Shiren, *Phys. Rev. Lett.* **36**, 888 (1976); R. L. Melcher and N. S. Shiren, *Phys. Lett. A* **57**, 377 (1976).
- ⁴⁴S. Kupca, I. Maartense, H. P. Kunkel, and C. W. Searle, *Appl. Phys. Lett.* **29**, 224 (1976).
- ⁴⁵K. Wilms, G. Vertogen, and G. A. Sawatzky, *Solid State Commun.* **20**, 1165 (1976).
- ⁴⁶K. Kajimura, K. Fossheim, T. G. Kazyaka, R. L. Melcher, and N. S. Shiren, *Phys. Rev. Lett.* **37**, 1151 (1976).
- ⁴⁷R. W. Gould, *Phys. Lett.* **19**, 477 (1965).
- ⁴⁸P. A. Fedders and E. Y. C. Lu, *Appl. Phys. Lett.* **23**, 502 (1973).
- ⁴⁹W. B. Mims, in *Electron Paramagnetic Resonance*, edited by S. Geschwind (Plenum, New York, 1972), p. 263.
- ⁵⁰G. F. Herrmann and R. F. Whitmer, *Phys. Rev.* **143**, 122 (1966).
- ⁵¹Robert M. White, *J. Appl. Phys.* **37**, 1693 (1966).
- ⁵²W. H. Kegel and R. W. Gould, *Phys. Lett.* **19**, 531 (1965).
- ⁵³F. W. Crawford and R. S. Harp, *J. Appl. Phys.* **37**, 4405 (1966).
- ⁵⁴B. A. Auld, *Acoustic Fields and Waves in Solids* (Wiley, New York, 1973).
- ⁵⁵H. F. Tiersten, *Linear Piezoelectric Plate Vibrations* (Plenum, New York, 1969).
- ⁵⁶R. P. Feynman, F. L. Vernon, Jr., and R. W. Hellwarth, *J. Appl. Phys.* **10**, 221 (1967).
- ⁵⁷G. F. Herrmann, R. M. Hill, and D. E. Kaplan, *Phys. Rev.* **156**, 118 (1967).
- ⁵⁸G. F. Herrmann, D. E. Kaplan, and R. M. Hill, *Phys. Rev.* **181**, 829 (1969).
- ⁵⁹D. E. Kaplan, R. M. Hill, and G. F. Herrmann, *J. Appl. Phys.* **40**, 1164 (1969).
- ⁶⁰G. F. Herrmann, R. M. Hill, and D. E. Kaplan, *Phys. Rev. B* **2**, 2587 (1970).
- ⁶¹K. Kajimura, K. Fossheim, R. L. Melcher, and N. S. Shiren, presented at the Sixth International Conference on Internal Friction and Ultrasonic Attenuation in Solids, Tokyo, 1977.
- ⁶²In the VHF range our preliminary measurements and more extensive work by A. Levelut and coworkers (private communication) show rather extensive phase variations across the individual echoes.
- ⁶³Arnold L. Bloom, *Phys. Rev.* **98**, 1105 (1955).
- ⁶⁴S. Stokka and K. Fossheim (unpublished) have demonstrated that in KDP the temperature dependence of T_2^{-1} is unaffected by the applied field strength even though the magnitude of T_2^{-1} is itself field dependent.
- ⁶⁵L. R. Weisberg and J. Blanc, *J. Appl. Phys.* **34**, 1002 (1963).
- ⁶⁶H. J. McSkimin, A. Jayaraman, and P. Andreatch, Jr., *J. Appl. Phys.* **38**, 2362 (1967).
- ⁶⁷N. S. Shiren and R. L. Melcher, presented at the 1976 IEEE Ultrasonic Symposium, Paper No. K-5.

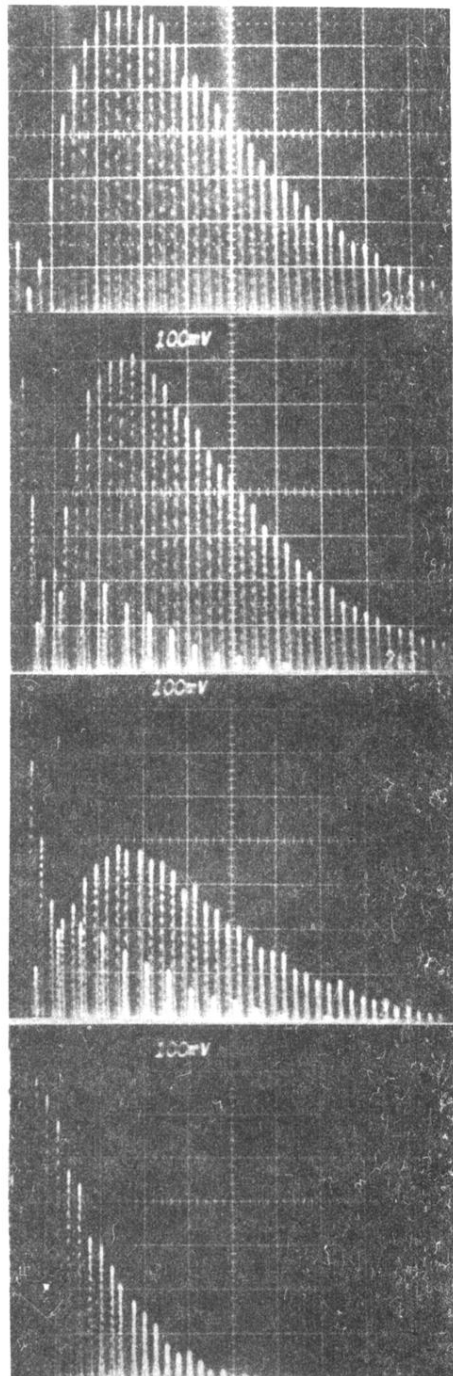


FIG. 36. Echo decay envelopes for various E_2 with $E_1 = -24$ dB. 3τ echoes are easily distinguished on the second and third pictures. Time scale is $\tau = 2\mu\text{s}/\text{cm}$ (not 2τ). Top to bottom: $E_2 = -42, -33, -26,$ and -20 dB. ZnO: 8.6 GHz, 1.25 K, $\Delta_1 = \Delta_2 = 100$ ns.

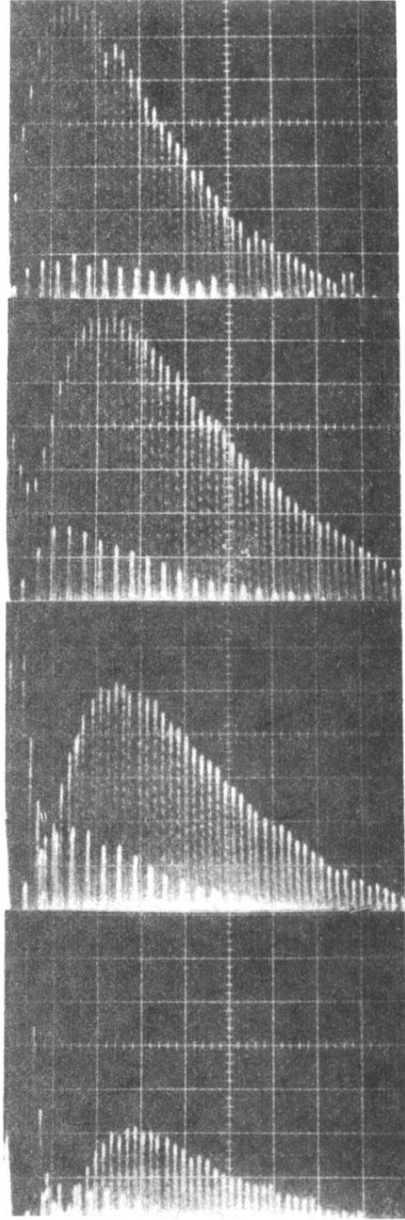


FIG. 39. Decay envelopes for various E_1 with E_2 maintained 5 dB below E_1 . 3τ echoes are also observable. Time scale: $\tau = 2 \mu\text{s}/\text{cm}$. Top to bottom: $E_1 = -40, -25, -22,$ and -19 dB. ZnO: 8.6 GHz, 1.25 K, $\Delta_1 = \Delta_2 = 100$ ns.

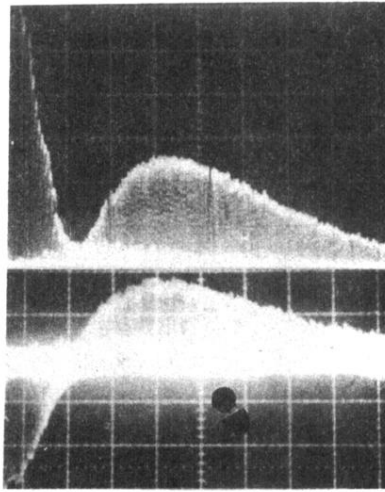


FIG. 42. e_2 vs τ with E_1 5 dB greater than E_2 . ZnO: 1.25 K, 9.0 GHz, $\Delta_1 = \Delta_2 = 50$ ns. Top: amplitude detection. Bottom: phase-sensitive detection adjusted for zero phase on the second-envelope maximum.

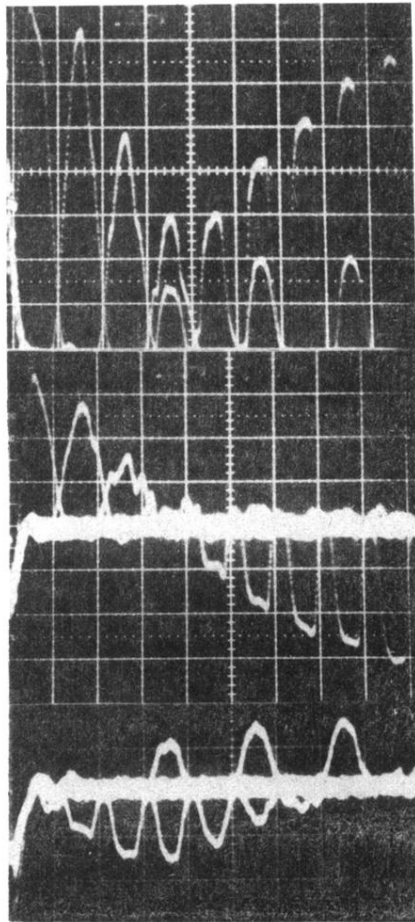


FIG. 43. ϕ_2 vs τ for E_1 6 dB greater than E_2 in the neighborhood of the envelope minimum ZnO: 1.25 K, 9.06 GHz, $\Delta_1 = \Delta_2 = 300$ ns. Top: amplitude detection. Middle: phase-sensitive detection adjusted for zero phase on the second-envelope maximum. Bottom: phase-sensitive detection with reference 90° out of phase with that above. 3τ echoes are distinguishable by their larger interecho spacing.

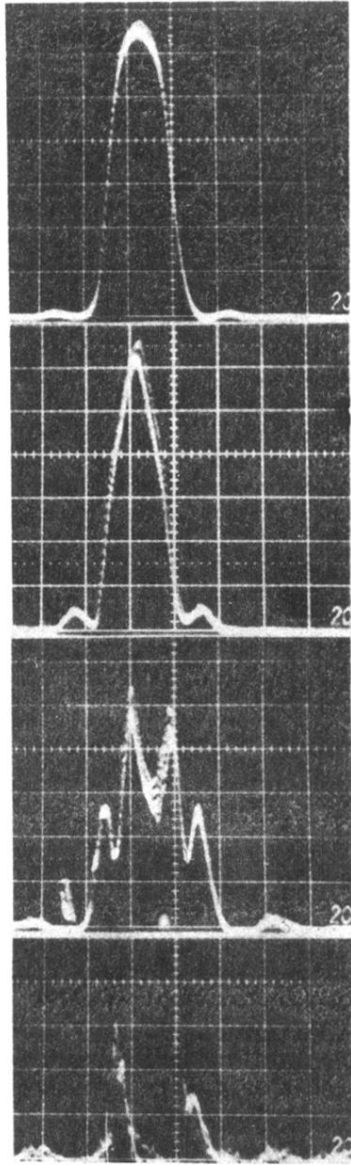


FIG. 44. Representative echo shapes for $\Delta_1 = 300$ ns and various Δ_2 . τ slightly greater than τ_d ($\Delta_2 = 300$ ns). E_1 3 dB greater than E_2 . ZnO: 8.8 GHz, 1.25 K. Top to bottom: $\Delta_2 = 300, 200, 100,$ and 50 ns.

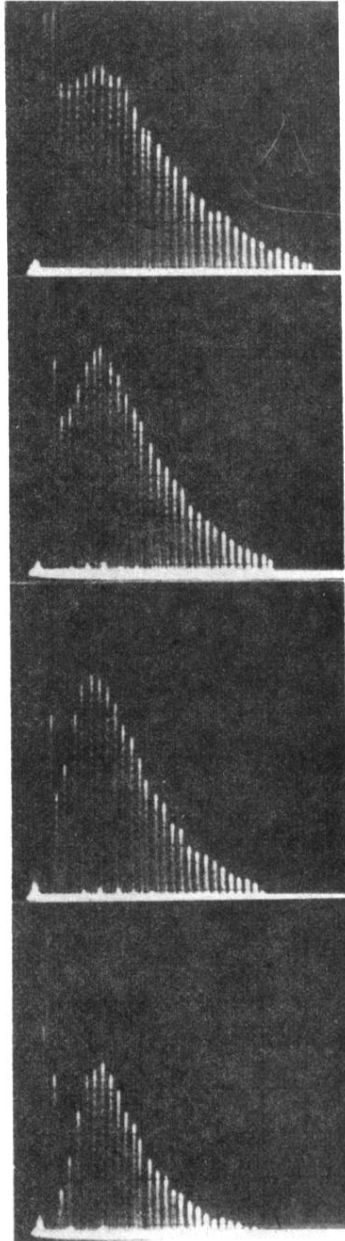


FIG. 46. Decay envelopes with E_1 8 dB greater than E_2 and $\Delta_1 = \Delta_2 = 100$ ns, for various temperatures. Top to bottom: $T = 1.25, 2.5, 3,$ and 3.5 K. ZnO: 17 GHz, $2 \mu\text{s}/\text{cm}$.

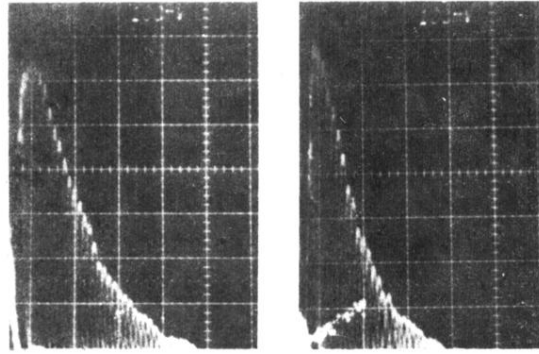


FIG. 51. Echo-decay envelopes at 9 K and E_1 5 dB greater than E_2 . Time scale: 500 ns/cm. Left: $E_1 = -8$ dB. Right: $E_1 = -20$ dB. ZnO: 8.6 GHz, $\Delta_1 = \Delta_2 = 100$ ns.

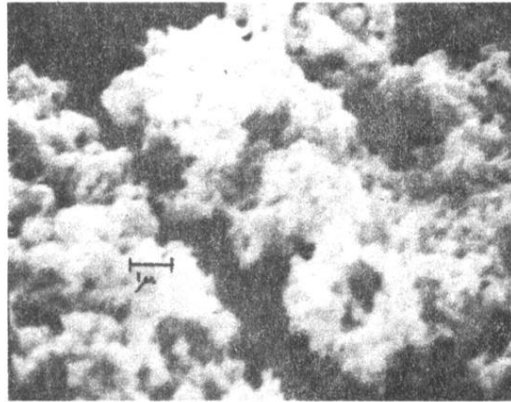


FIG. 6. Electron micrograph of ZnO powder utilized in X - Ku band-echo measurements.

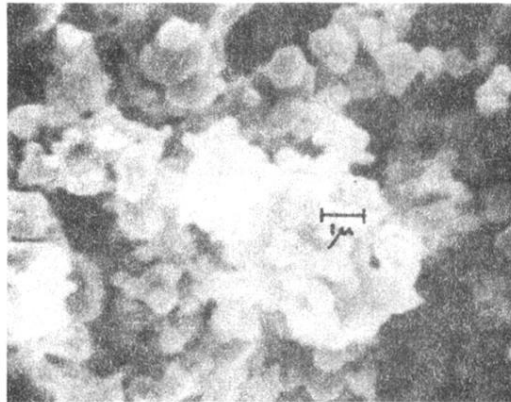


FIG. 7. Electron micrograph of a ZnO powder which did not show echoes at X - Ku band frequencies.